

# First results of scientific performance for the design of ESA space based gravitational wave detector (*ELISA*)

*The Science Performance Task Force (SPTF):* Pau Amaro-Seoane<sup>1</sup>, Sofiane Aoudia<sup>1</sup>, Gérard Auger<sup>2</sup>, Stanislav Babak<sup>1</sup>, Emanuele Berti<sup>3</sup>, Neil J. Cornish<sup>4</sup>, Jonathan Gair<sup>5</sup>, Oliver Jennrich<sup>6</sup>, Philippe Jetzer<sup>7</sup>, Ioannis Kamaretsos<sup>8</sup>, Antoine Klein<sup>7</sup>, Ryan Lang<sup>9</sup>, Tyson Littenberg<sup>9</sup>, Sean T. McWilliams<sup>10</sup>, Gijs Nelemans<sup>11</sup>, Frank Ohme<sup>1</sup>, Antoine Petiteau<sup>1</sup>, Eric Plagnol<sup>2</sup>, Edward K. Porter<sup>2</sup>, Emma Robinson<sup>1</sup>, B. S. Sathyaprakash<sup>9</sup>, Bernard Schutz<sup>1</sup>, Alberto Sesana<sup>1</sup>, Carlos Sopuerta<sup>12</sup>, Alessandro Spallicci<sup>13</sup>, James I. Thorpe<sup>9</sup>, Michele Vallisneri<sup>14,15</sup>, Alberto Vecchio<sup>16</sup>, Marta Volonteri<sup>17</sup>

<sup>1</sup> Max-Planck-Institut für Gravitationsphysik (Albert-Einstein-Institut), Am Mühlenberg 1, D-14476 Golm bei Potsdam, Germany

<sup>2</sup> APC, UMR 7164, Univ. Paris 7 Denis Diderot, 10, rue Alice Domon et Leonie Duquet, 75025 Paris Cedex 13, France

<sup>3</sup> University of Mississippi, USA

<sup>4</sup> Dept. of Physics, Montana State Univ., Bozeman, MT 59717, USA

<sup>5</sup> Inst. of Astronomy, Univ. of Cambridge, Madingley Rd., Cambridge, CB30HA, UK

<sup>6</sup> European Space Agency

<sup>7</sup> Institute of Theoretical Physics, University of Zurich

<sup>8</sup> School of Physics and Astronomy, Cardiff Univ., 5, The Parade, Cardiff, CF243YB, UK

<sup>9</sup> Gravitational Astrophysics Lab., NASA Goddard Space Flight Center, 8800 Greenbelt Rd., Greenbelt, MD 20771, USA

<sup>10</sup> Department of Physics, Princeton University, Princeton, NJ 08544, USA

<sup>11</sup> Department of Astrophysics, Radboud University Nijmegen, The Netherlands

<sup>12</sup> Institute of Space Sciences (ICE-CSIC), Barcelona, Spain

<sup>13</sup> University of Orleans, France

<sup>14</sup> Jet Propulsion Laboratory, California Inst. of Technology, Pasadena, CA 91109, USA

<sup>15</sup> Theoretical Astrophysics, California Inst. of Technology, Pasadena, CA 91125

<sup>16</sup> School of Physics and Astronomy, Univ. of Birmingham, Edgbaston, Birmingham B152TT, UK

<sup>17</sup> University of Michigan

E-mail: Antoine.Petiteau@aei.mpg.de, porter@apc.univ-paris7.fr

## Abstract.

This document collects the current results of science performance studies of potential configurations for the "new LISA".

## Contents

<b>1</b>	<b>Instrument configurations : noises, orbits and sensitivity</b>	<b>3</b>
1.1	Overview . . . . .	3
1.2	Noises . . . . .	3
1.2.1	Acceleration noises . . . . .	3
1.2.2	Shot noise . . . . .	4
1.2.3	Other measurement noises . . . . .	5
1.2.4	Laser noise . . . . .	5
1.3	Orbits . . . . .	5
1.3.1	LISA like orbits . . . . .	5
1.3.2	Halo around L1 . . . . .	6
1.4	Noise power spectral density (PSD) . . . . .	8
1.4.1	Analytical model . . . . .	8
1.4.2	Simulation . . . . .	9
1.5	Sensitivity . . . . .	9
1.5.1	Analytical model . . . . .	9
1.5.2	Simulation . . . . .	10
<b>2</b>	<b>Science return for Galactic Binaries</b>	<b>10</b>
2.1	Methodology . . . . .	11
2.2	Results . . . . .	12
2.2.1	Confusion Noise . . . . .	12
2.2.2	Recovered Source Catalogue . . . . .	12
2.2.3	Verification Binaries . . . . .	13
<b>3</b>	<b>Massive Black Hole binaries</b>	<b>16</b>
3.1	Cosmological populations of massive black hole binaries ( <i>Alberto Sesana &amp; Marta Volonteri</i> )	16
3.2	Massive black hole formation and evolution models . . . . .	17
3.2.1	Details of the merger tree implementation . . . . .	18
3.2.2	Detailed content of the files . . . . .	19
3.3	Parameter estimation . . . . .	24
3.3.1	Averaged SNRs and horizon distances ( <i>Emanuele Berti, Neil Cornish, &amp; Stas Babak</i> )	24
3.3.2	Results using inspiral waveform with spin precession and higher harmonics ( <i>Ryan Lang &amp; Neil Cornish</i> )	25
3.3.3	Results using inspiral waveform with spin precession and higher harmonics ( <i>Antoine Petiteau, Sofiane</i>	26
3.3.4	Inspiral-Merger-Ringdown with higher harmonics (EOB based) ( <i>Sean McWilliams</i> )	32
3.3.5	Results using inspiral waveform with higher harmonics ( <i>Ed Porter</i> )	33
3.3.6	Results using ringdown phase ( <i>Ioannis Kamaretsos, B.Sathyaprakash</i> )	33
3.3.7	Results using PhenomC (Inspiral-Merger-Ringdown) from AEI ( <i>Stas Babak, Antoine Petiteau, Alberto</i>	34
3.4	4 vs 6 links and low frequency sensitivity impact on the source distance determination ( <i>A. Sesana</i> )	43
3.5	Model selection ( <i>Alberto Sesana, Marta Volonteri, Emanuele Berti, Jonathan Gair</i> )	46
<b>4</b>	<b>Model Selection</b>	<b>46</b>
<b>5</b>	<b>Observable population and crude error estimation.</b>	<b>47</b>
<b>6</b>	<b>EMRIs</b>	<b>52</b>

## 1. Instrument configurations : noises, orbits and sensitivity

(‘section captain’ : Antoine Petiteau)

### 1.1. Overview

During the ”first phase” (before CDF), 6 configurations had been defined. The table 1 gives a summary of their main characteristics and the induced noise levels.

Configuration	C5	C4	C3	C2	C1	HL1
Armlength ( $\times 10^9$ m)	2	3	1	1	1	1 - 1.6
Orbits	analytic	analytic	analytic	$10^\circ$	closest	$20^\circ$
Diameter telescope (m)	0.28	0.25	0.25	0.4	0.4	0.25
Laser power (W)	2	0.7	0.7	2	0.05	0.7
Acceleration system	DRS	DRS	DRS	DRS	LPF <sup>(1)</sup>	DRS
Acceleration ( $10^{-48} f^{-2} \text{Hz}^{-1}$ )	6	6	6	6	$8.2 \left(1 + \frac{1.8 \times 10^4}{f^2}\right)^2$	6
Shot noise ( $10^{-38} f^2 \text{Hz}^{-1}$ )	2.05	20.07	2.31	$0.06^{(2)}$	4.92	2.31
Fixed noise ( $10^{-38} f^2 \text{Hz}^{-1}$ )	2.81	2.81	2.81	2.81	2.81	2.81

Table 1: Summary of configuration. Noises are given in  $\delta\nu/\nu$  unit.

### 1.2. Noises

The noise models used for the new space-based gravitational wave detector supported by ESA have been provided by ESA. Each noise includes the standard ESA margin  $M_{ESA} = 1/0.65$ .

In the following description, we give the general formulation of the root mean square value (RMS), i.e. square root of the power spectral density (PSD) in the standard unit of the noise. We also give the value used for each configurations in relative frequency unit  $\frac{\delta\nu}{\nu}$ .

The conversion between rms noise,  $\delta x$ , and power spectral density  $S$  is :  $S = \delta x^2$ .

The conversion between acceleration noise unit (in  $\text{m}^2.\text{s}^{-4}.\text{Hz}^{-1}$ ) and noise in length unit (in  $\text{m}^2.\text{Hz}^{-1}$ ) is :

$$S(f) = S_{\text{m}^2.\text{s}^{-4}.\text{Hz}^{-1}}(f)/(2\pi f)^4 \text{m}^2.\text{Hz}^{-1} \quad (1)$$

The conversion between noise in length unit ( $\text{m}^2.\text{Hz}^{-1}$ ) and noise in relative frequency unit (in  $\text{Hz}^{-1}$ ) is :

$$S_{\frac{\delta\nu}{\nu}}(f) = S(f) \times \left(\frac{2\pi f}{c}\right)^2 \text{Hz}^{-1} \quad (2)$$

**1.2.1. Acceleration noises** This noise is due to the limitation of the drag-free system. We consider two types of acceleration noise :

- DRS : acceleration noise corresponding to LISA requirements :

$$\delta x_{\text{acc}}^{\text{DRS}} = M_{ESA} \times 3 \times 10^{-15} \text{m/s}^2/\sqrt{\text{Hz}} \quad (3)$$

- LPF : acceleration noise corresponding to LISAPathfinder :

$$\delta x_{\text{acc}}^{\text{LPF}} = M_{\text{ESA}} \times 3.5 \times 10^{-15} \left( 1 + \frac{0.18 \text{ mHz}}{f} \right) \text{m/s}^2/\sqrt{\text{Hz}} \quad (4)$$

So, we have one best case, the DRS, and one worth case, the LPF.

Note that for the LPF noise, we include the ESA margin but, according to Stefano Vitale, the margin was already taken into account in the  $3.5 \times 10^{-15}$  value. So the LPF acceleration was over-estimated (only used for configuration C1).

The acceleration noise for the different configurations is :

- for C1 :

$$S_{\text{acc}, \frac{\delta \nu}{\nu}}(f) = 8.17 \times 10^{-48} \left( \frac{1}{f} + \left( \frac{1.8 \times 10^{-4}}{f^2} \right) \right)^2 \text{Hz}^{-1} \quad (5)$$

- for C2, C3, C4, C5, HL1 :

$$S_{\text{acc}, \frac{\delta \nu}{\nu}}(f) = 6.00 \times 10^{-48} f^{-2} \text{Hz}^{-1} \quad (6)$$

*1.2.2. Shot noise* This noise depends directly on the received laser power after the travel between two spacecrafts. Therefore it depends on :

- $L$  : the armlength (in m ),
- $D$  : the diameter of the telescope (in m),
- $P$  : the emitted laser power (in Watt)

$$\delta x_{\text{SN}} = M_{\text{ESA}} \times 7.7 \times 10^{-12} \left( \frac{1 \text{ W}}{P} \right)^{1/2} \left( \frac{L}{5 \times 10^9 \text{ m}} \right) \left( \frac{0.4 \text{ m}}{D} \right)^2 \text{m}/\sqrt{\text{Hz}} \quad (7)$$

The acceleration noise for the different configurations is :

- for C1 :

$$S_{\text{SN}, \frac{\delta \nu}{\nu}}(f) = 4.92 \times 10^{-38} f^2 \text{Hz}^{-1} \quad (8)$$

- for C2 :

$$S_{\text{SN}, \frac{\delta \nu}{\nu}}(f) = 6.14 \times 10^{-40} f^2 \text{Hz}^{-1} \quad (9)$$

- for C3 :

$$S_{\text{SN}, \frac{\delta \nu}{\nu}}(f) = 2.31 \times 10^{-38} f^2 \text{Hz}^{-1} \quad (10)$$

- for C4 :

$$S_{\text{SN}, \frac{\delta \nu}{\nu}}(f) = 2.07 \times 10^{-37} f^2 \text{Hz}^{-1} \quad (11)$$

- for C5 :

$$S_{\text{SN}, \frac{\delta \nu}{\nu}}(f) = 2.05 \times 10^{-38} f^2 \text{Hz}^{-1} \quad (12)$$

- for HL1 :

$$S_{\text{SN}, \frac{\delta \nu}{\nu}}(f) = 2.31 \times 10^{-38} f^2 \text{Hz}^{-1} \quad (13)$$

*1.2.3. Other measurement noises* This noise groups to the perturbation of the optical path in the optical bench and the telescope and the precision on the interference measurement by the photodiode and the phasemeter.

$$\delta x_{\text{OMS}} = M_{\text{ESA}} \times 6.2 \times 10^{-12} \text{m} / \sqrt{\text{Hz}} \quad (14)$$

The other measurement noise is the same for all the configurations :

- for C1, C2, C3, C4, C5, HL1 :

$$S_{\text{OMS}, \frac{\delta \nu}{\nu}}(f) = 2.81 \times 10^{-38} f^2 \text{Hz}^{-1} \quad (15)$$

*1.2.4. Laser noise* The laser noise which have a typical rms noise around  $30 \text{ Hz} \cdot \text{Hz}^{-1/2}$  is reduced by the Time Delay Interferometry method. For this study, we suppose that the application of TDI second generation reduce the laser noise below the other noise. So it will not be consider.

### 1.3. Orbits

We use several spacecraft orbits divided in 2 types : LISA like orbits and Halo around Lagrange point L1. There are 2 key points :

- the stability of the constellation which have implication to the mission duration and on the shot noise level (see 1.2.2).
- the way of reaching the orbits which have direct budget link through the energy required

*1.3.1. LISA like orbits* The LISA like orbits corresponds to constellation in a pseudo-equilateral triangle. The barycenter of the constellation follows the Earth with a certain Earth-detector barycenter angle,  $\theta_{\text{EdB}}$ . For this type of orbits, the constellation 2 key points are the armlength and the angle  $\theta_{\text{EdB}}$ . To keep the stability, if we want to increase the armlength, it implies an increase of  $\theta_{\text{EdB}}$  for limiting the tidal deformation due to the Earth.

We test 2 orbits which are the output of numerical simulation done by Oliver Jennrich (ESA) :

- best case :  $\theta_{\text{EdB}} = 10^\circ$  and  $L = 10^9 \text{ m}$ ,
- worst case : closest to the Earth ( $\theta_{\text{EdB}} = ??^\circ$ ) and  $L = 10^9 \text{ m}$ ,

We also use the standard analytical LISA orbits from [1] changing the armlength.

The figure 1 shows the numerical orbits compared to the analytic orbits with  $L = 10^9 \text{ m}$ . Regarding the position of the spacecraft the numerical orbits are close to the analytic ones. This means that the analytic orbits are a good approximation to the numeric one for computing the response of the detector to gravitational waves.

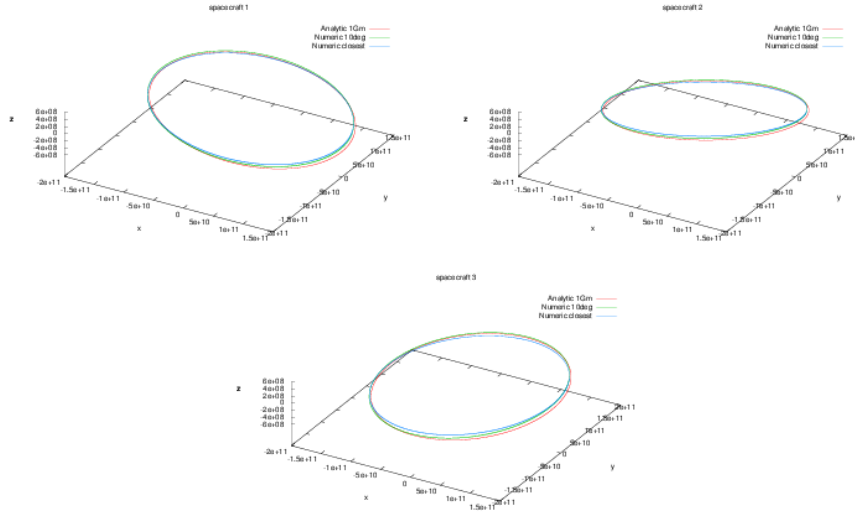


Figure 1: Orbits of the 3 spacecrafts.

The main difference between this orbits is the time variation of the armlength as shown on the figure ???. This is an important point for the technological design of the detector (Doppler effect, ...) and for the application of the Time Delay Interferometry which is the pre-data-analysis method for reducing the laser noise.

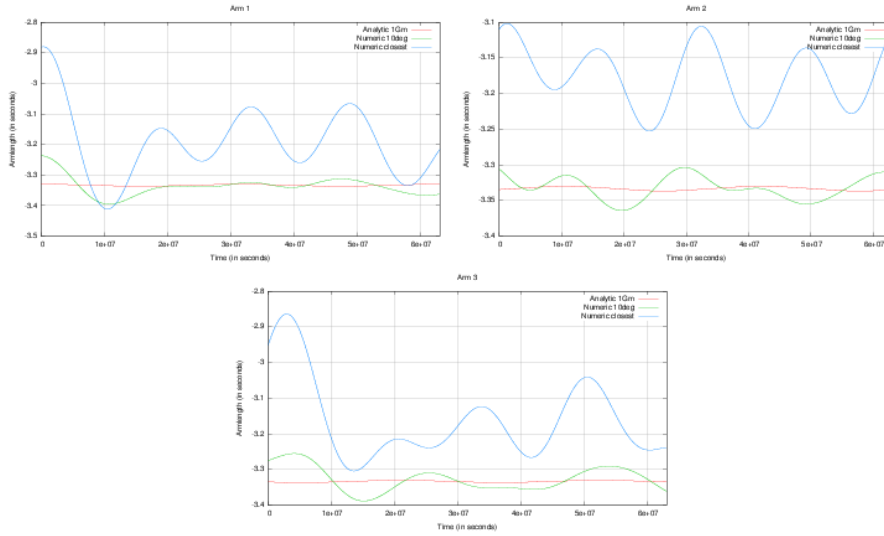


Figure 2: Time evolution of the 3 armlength during 2 years.

**1.3.2. Halo around L1** We test another kind of orbits : the Halo around Lagrange point L1. This orbits are the results of numerical simulation done by Vitali Mueller (AEI-Hannover). It's a mother/daughter configuration : there are only 4 links (2

arms). The figure 3 shows the orbits and the figure 4 shows the armlength evolution.

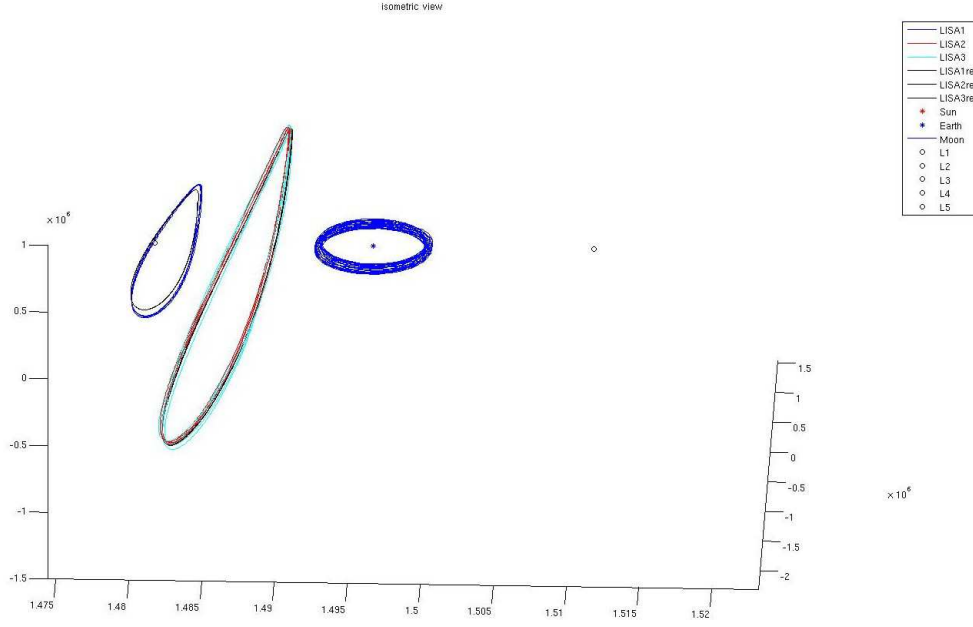


Figure 3: Orbits of spacecraft for the Halo around L1 configuration.

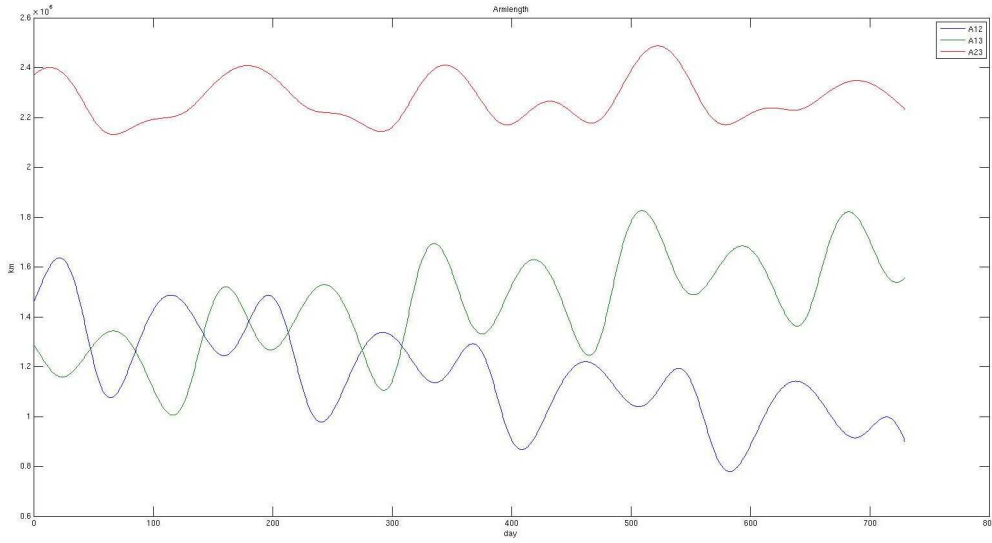


Figure 4: Evolution of armlength for the Halo around L1 configuration.

The main spacecraft (mother) is on a close orbit around L1 and the 2 daughters are on a distant orbits separated in phase by  $\pi$ . The angle between the 2 arms is around  $120^\circ$ . The armlengths evolve between 1 and 1.6 million km.

#### 1.4. Noise power spectral density (PSD)

1.4.1. *Analytical model* The analytic formulation of the Power Spectral Density of TDI X can be approximated by (usual approximation used in LISA) :

$$S_{n,\frac{\delta\nu}{\nu}}^X(f) = 16 \sin^2(\phi_L(f)) \left( S_{SN,\frac{\delta\nu}{\nu}}(f) + S_{OMN,\frac{\delta\nu}{\nu}}(f) + (3 + \cos(2\phi_L(f))) S_{acc,\frac{\delta\nu}{\nu}}(f) \right) \quad (16)$$

with  $\phi_L(f) = 2\pi fL/c$

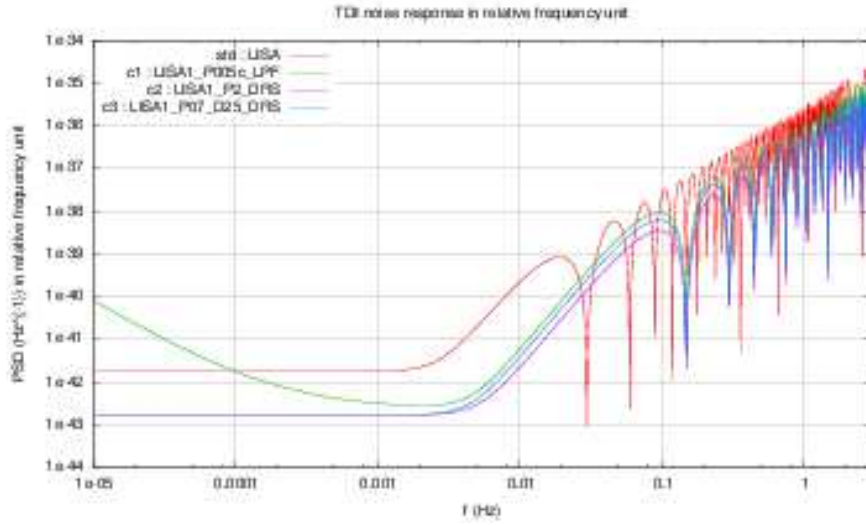


Figure 5: Comparison of power spectral density of noises' response for standard LISA, configurations 3a, 4a and 5a



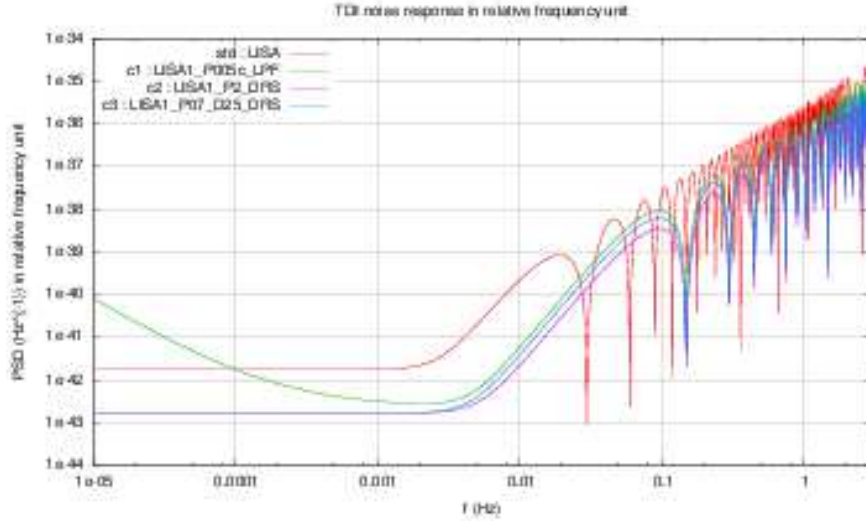


Figure 6: Comparison of power spectral density of noises' response for standard LISA, configurations 1c, 2 and 3

#### 1.4.2. Simulation

#### 1.5. Sensitivity

1.5.1. *Analytical model* (Very) approximative analytic formulation (based on LISA science requirements document (2010)) :

The transfert function is

$$T(f) = \sqrt{1 + \left( \frac{f}{(0.41 \left( \frac{c}{2L} \right))} \right)^2} \quad (17)$$

Sensitivity formulation :

$$\sqrt{S_h^X}(f) = \sqrt{5} \frac{2}{\sqrt{3}} T(f) \frac{\sqrt{4S_{acc} + S_{SN} + S_{omn}}}{L} \quad (18)$$

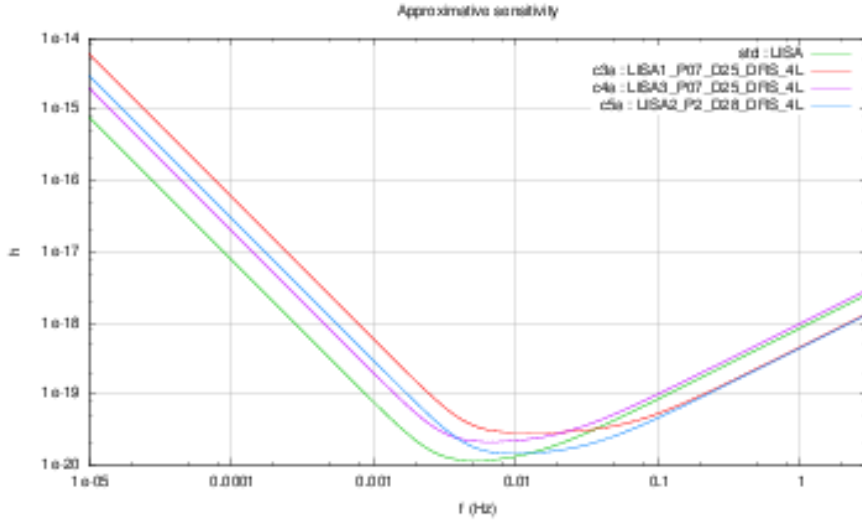


Figure 7: Comparison of sensitivity (SNR=1, "instantaneous") for standard LISA, configurations 3a, 4a and 5a

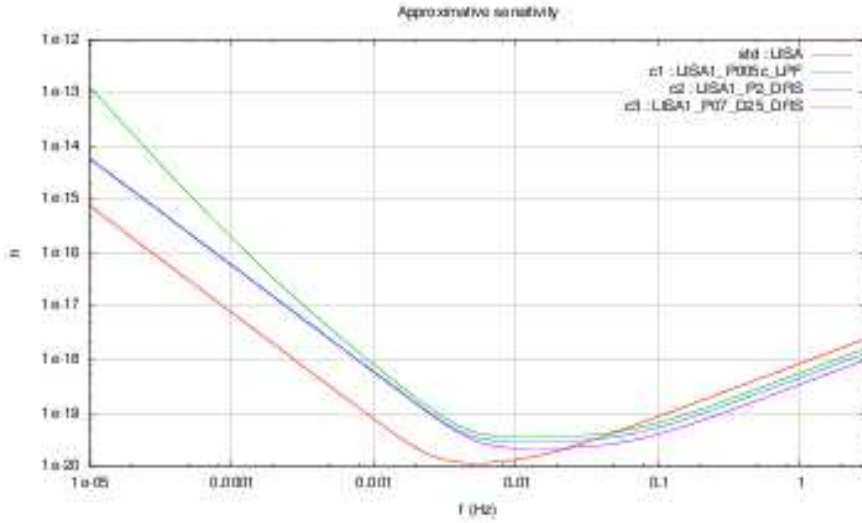


Figure 8: Comparison of sensitivity (SNR=1, "instantaneous") for standard LISA, configurations 1c, 2 and 3

### 1.5.2. Simulation

## 2. Science return for Galactic Binaries

(*'section captain'* : Tyson Littenberg)

Here we summarize the detection capabilities for Galactic Binaries with different ELISA configurations.

### 2.1. Methodology

The galactic confusion estimation is performed using the `GB_confusion` package of codes which have been incorporated into `lisatools/MLDCwaveforms`. Included in the directory on the SVN repository are example files, run scripts and a (readable?) README.

To estimate the confusion noise we first simulate the instrument response to the galactic foreground by generating and co-adding waveforms for each source in the simulated galaxy downloaded from

<https://lisa-light.aei.mpg.de/bin/view/GalacticBinaries/PopulationGalacticBinaries>

The `GB_confusion` codes expect the source catalogue to be in the “MLDC” file format, i.e. with columns

$$f_0, \dot{f}_0, \theta, \phi, \mathcal{A}_0, \iota, \psi, \varphi_0.$$

Parameters  $f$  is the GW frequency, subscript 0 denotes values measured at the start of the mission observation,  $\{\theta, \phi\}$  are the ecliptic latitude and longitude of the source in radians,  $\mathcal{A}$  is the amplitude, and  $\{\iota, \psi, \varphi_0\}$  are the inclination, polarization, and initial wave phase, together describing the orientation of the binary with respect to the line of sight from the solar system barycenter (SSB). The `PopulationGalacticBinaries` sources are parameterized by their orbital period (and  $\dot{P}$ ), the component masses of the binary, the luminosity distance, and the sky-location in galactic coordinates, so the appropriate conversions need to be applied *a priori*. Also, the supplied galaxy simulations are over-populated with interacting binaries (those with  $\dot{f}_0 < 0$  by a factor of  $\sim 10$ . We account for this by randomly culling 90% of mass-transferring binaries from the population before computing the instrument response. While the TDI signals from the galaxy are being simulated, any binaries with signal-to-noise ratio (SNR) greater than one are stored in a separate “Brights” file which will later analyzed to determine which are detectable.

With the simulated data in hand, we iteratively estimate the confusion noise by dividing the Fourier domain data into  $\sim 30$  segments between  $\sim 10^{-4}$  and  $\sim 10^{-1}$  Hz and compute the median Fourier power in each segment. The SNR for each signal in the Brights file is computed against this confusion noise (plus instrument noise), and any with signal-to-noise greater than 7 are stored as “detectable” and removed from the data. This process is repeated iteratively until the confusion estimation converges. The analysis is performed simultaneously considering 4- and 6-link configurations, producing separate results for the Michelson “X” channel (4 links) and noise orthogonal “AET” channels (6 links).

To understand the parameter estimation capabilities of different configurations, the lower-bound on the uncertainties for each source’s parameters are computed using the Fisher Information Matrix (FIM), using the instrument + confusion noise as the weighting in the inner products. We separately report on the number of signals w/  $\dot{f}$  measured w/in 20% as a proxy for number with measurable  $D_L$ . Using only  $\dot{f}$  to disentangle the distance from the overall amplitude implicitly assumes that the binary’s dynamics are dominated by the radiation reaction force. To unequivocally verify this assumption, we also need to measure the second time derivative of the frequency which was a difficult task even for LISA.

## 2.2. Results

**2.2.1. Confusion Noise** The confusion noise estimates for each configuration under consideration are shown in Figure 9. The green [dashed] traces show the instrument noise. The red [solid] curves are the full noise spectra with confusion noise included, illustrating the impact of the astrophysical foreground on the instrument sensitivity. The black [dotted] lines are the LISA baseline instrument noise, and are included for reference. All estimates are for two year observation times. The confusion noise does not have a significant impact on the detector sensitivity for the 1 Gm configurations.

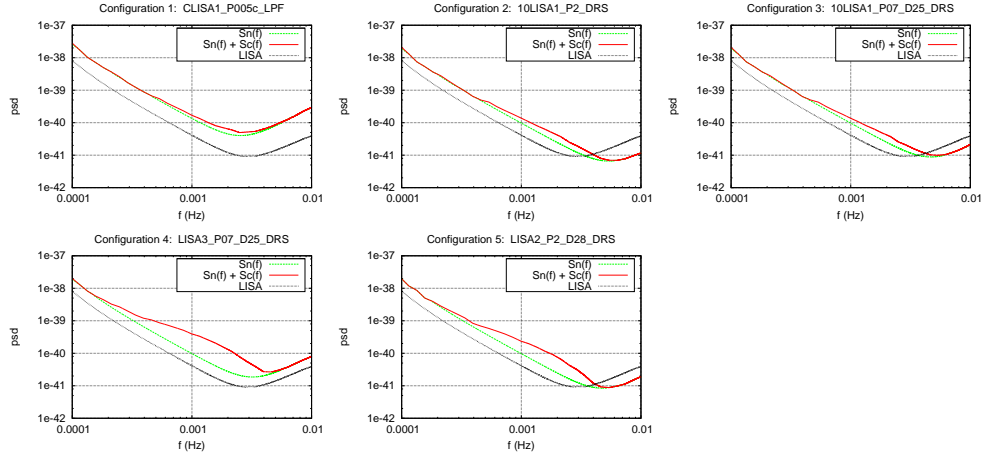


Figure 9: Noise spectra for different detector configurations. The red [solid] curves show the full noise spectrum, the green [dashed] curves are the instrument-only noise spectra and the black [dotted] line is the baseline LISA instrument noise curve. All results are for two year mission lifetimes.

**2.2.2. Recovered Source Catalogue** Here we use the lists of detectable binaries and the FIM to make very coarse statements about the science potential for the different configurations. Table 2 summarizes the parameter estimation results. Of the total number of detectable binaries (shown in the  $\text{SNR} > 7$  column of the table), the number of which that can be resolved on the sky to  $\lesssim 1 \text{ deg}^2$  are separately tabulated. This number ranges between a few hundred to  $\sim 2000$  for the most sensitive configuration. Binaries with a fractional error in  $\dot{f}_0$  of less than 20% are of particular interest, as the frequency evolution can be used to constrain the luminosity distance to the source. Perhaps the most astrophysically interesting number is in the final column of Table 2, which shows the number of detectable binaries that are both well localized in the sky and have potentially well constrained luminosity distances. It is from this sub-population of detectable binaries that the 3D spatial distribution of the Galaxy can be directly probed. The bottom row of the table shows the results for the baseline LISA design.

The evaluation software also tracks the number of binaries with  $\ddot{f}_0$  constrained to within 20%. This quantity is required to unambiguously determine if the orbital period of the binary is being solely driven by the emission of gravitational waves, or if there is some additional dynamical interaction between two stars. Unfortunately, for the new configurations being considered, only a few binaries will have sufficiently

well constrained  $\ddot{f}$  during a two year observation time. This is not all that surprising, as the prospects for measuring  $\ddot{f}_0$  with LISA were uncertain at best.

	Detector Configurations	SNR > 7 4-link (6-link)	$\Delta\Omega \lesssim 1 \text{ deg}^2$ 4-link (6-link)	$\Delta\dot{f}/\dot{f} \leq 20\%$ 4-link (6-link)	$\{\theta, \phi, D_L\}$ 4-link (6-link)
1:	CLISA1_P005c_LPF	1071 (1846)	149 (387)	290 (469)	33 (55)
2:	10LISA1_P2_DRS	4586 (6204)	1107 (1892)	1331 (1678)	370 (457)
3:	10LISA1_P07_D25_DRS	4087 (5735)	932 (1679)	1176 (1510)	286 (357)
4:	LISA3_P07_D25_DR	7058 (12754)	1527 (2997)	1563 (2093)	465 (616)
5:	LISA2_P2_D28_DRS	6827 (11272)	1821 (3150)	1814 (2284)	628 (814)

Table 2: Summary of FIM parameter estimation results for the ensemble of detectable binaries for each configuration, considering both 6-link and 4-link operations. All results are for two year mission lifetimes.

*2.2.3. Verification Binaries* The parameter estimation capabilities of the “finalist” configurations (2,5) for the known verification binaries (VBs) are estimated using the Fisher Information Matrix. The FIM is computed for 1 000 realizations of each binary, Monte Carlo’ed over orientation. The inclination is drawn uniformly in  $\cos(\iota)$  over the range constrained by EM measurements [?]. For sources without well determined inclination angle (ES Cet and V407 Vul),  $\cos \iota$  is drawn from U[-1,1]. Consequently, these two sources show the largest spread in parameter estimation results. The binary source parameters, including ranges for inclination angle, can be found in Table 3.

Source	$f$ mHz	$\dot{f} \times 10^{-16}$ Hz/s	$\cos \theta$	$\phi$ rad	$\mathcal{A} \times 10^{-22}$	$\iota$ deg
RX J0806.3+1527	6.22028	-7.25472	-0.08212	2.10224	0.63782	38–39
HP Lib	1.81324	0	0.08665	4.10305	1.76277	26–34
SDSS J0651+2844	2.61301	0	0.10132	1.76872	1.66997	85.9–88.5
AM CVn	1.94414	0	0.65349	2.97383	1.50933	41–45
ES Cet	3.22061	0	-0.35488	0.42962	0.53591	0–180
V407 Vul	3.51250	-0.19555	0.81654	5.14867	0.32957	0–180
V803 Cen	1.25313	0	-0.52905	3.77284	1.36368	12–15
CR Boo	1.35962	0	0.31234	3.53028	1.07345	30–31

Table 3: Verification binary parameters.

The FIM results are shown in Figures 10 – 14. The analysis was repeated where we take the sky-location to be known exactly. While knowledge of the sky-location and frequency *a priori* makes detection significantly easier, breaking the correlations between these and the other parameters tabulated here account for differences at the 10% level or below, and so are omitted.

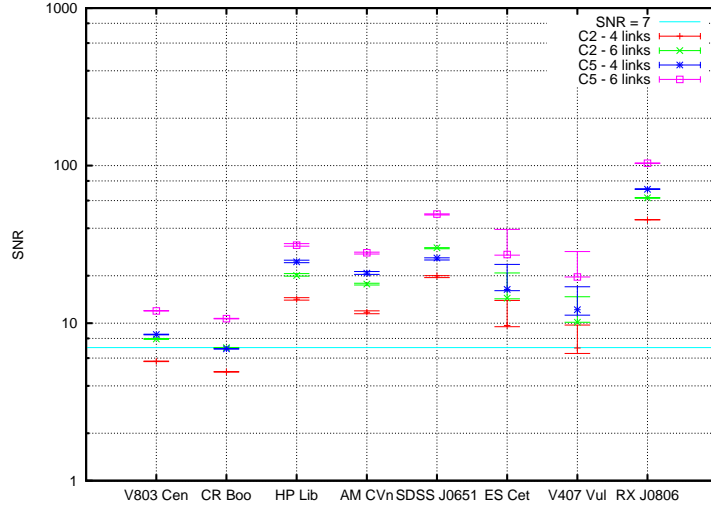


Figure 10: SNR of detectable verification binaries for Config 1 and 2, 4 and 6 links. Error bars represent the full range of values from 1000 realizations of each binary Monte Carlo'ed over orientation. The marked point represents the mode of the distribution. The ranges for each binary's inclination angle can be found in Table 3.

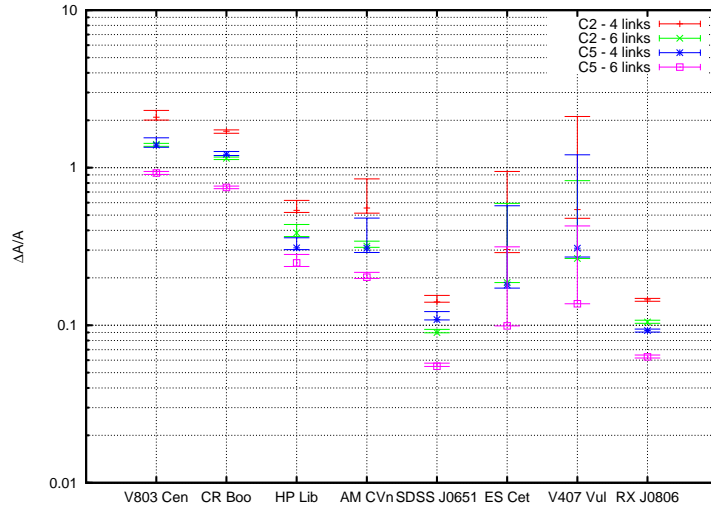


Figure 11: Fractional error in amplitude of detectable verification binaries for Config 1 and 2, 4 and 6 links. Error bars represent the full range of values from 1000 realizations of each binary Monte Carlo'ed over orientation. The marked point represents the mode of the distribution. The ranges for each binary's inclination angle can be found in Table 3.

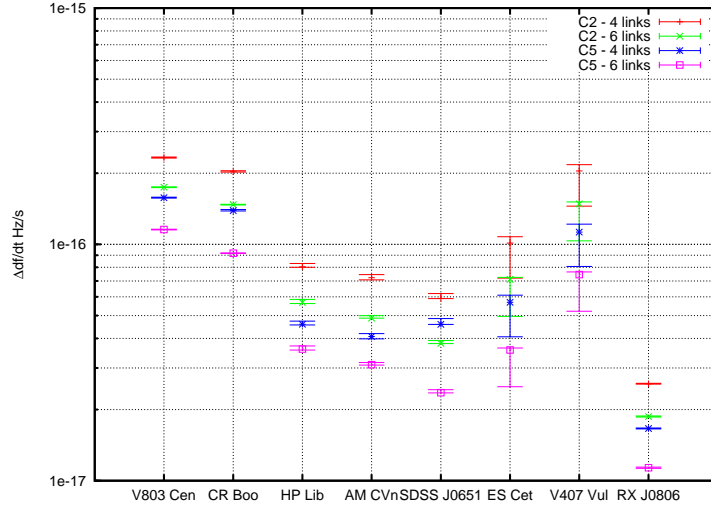


Figure 12: Error in  $\dot{f}$  of detectable verification binaries for Config 1 and 2, 4 and 6 links. Error bars represent the full range of values from 1000 realizations of each binary Monte Carlo'd over orientation. The marked point represents the mode of the distribution. The ranges for each binary's inclination angle can be found in Table 3.

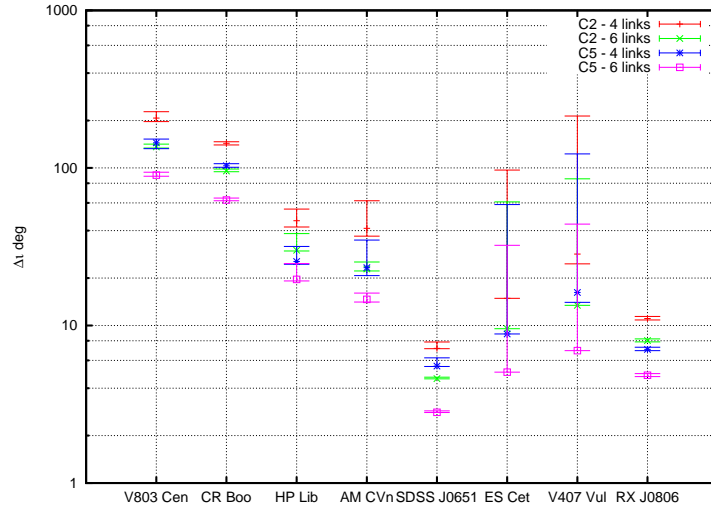


Figure 13: Inclination error of detectable verification binaries for Config 1 and 2, 4 and 6 links. Error bars represent the full range of values from 1000 realizations of each binary Monte Carlo'd over orientation. The marked point represents the mode of the distribution. The ranges for each binary's inclination angle can be found in Table 3.

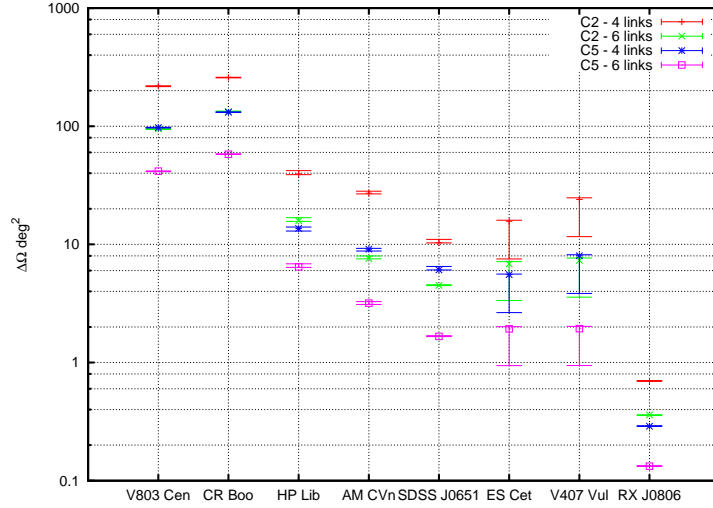


Figure 14: Angular resolution for detectable verification binaries for Config 1 and 2, 4 and 6 links. Error bars represent the full range of values from 1000 realizations of each binary Monte Carlo’ed over orientation. The marked point represents the mode of the distribution. The ranges for each binary’s inclination angle can be found in Table 3.

### 3. Massive Black Hole binaries

#### 3.1. Cosmological populations of massive black hole binaries (Alberto Sesana & Marta Volonteri)

This section contains the detailed description of the material included in this massive black hole binary population directory. We summarize the relevant physics of the models giving the appropriate references, and describe the content of each file column by column. We also include some sample figure to illustrate the relevant features of the binary populations. We provide 5 catalogues of binary mergers. The first four catalogues are meant to be used for Model Selection (we follow the naming convention used by the first LISAPE taskforce), the fifth catalogue is to be used for the Horizon estimation.

- **SE.** Small seeds, Efficient spin evolution. Model VHM, coherent accretion (aligned spins), gas driven dynamics (for eccentricity evolution);
- **SC.** Small seeds, Chaotic spin evolution. Model VHM, chaotic accretion (randomly oriented spins), star driven dynamics (for eccentricity evolution);
- **LE.** Large seeds, Efficient spin evolution. Model BVR, coherent accretion (aligned spins), gas driven dynamics (for eccentricity evolution);
- **LC.** Large seeds, Chaotic spin evolution. Model BVR, chaotic accretion (randomly oriented spins), star driven dynamics (for eccentricity evolution).
- **HOR:** an ‘average’ model, constructed by summing up the distributions  $d^3N_i/dM_z dq dz$  (being  $M_z$  the total redshifted binary mass and  $q = M_2/M_1 < 1$  the binary mass ratio) and dividing by four. This model should be used for the ‘horizon determination’ of the new gravitational wave detector.



### 3.2. Massive black hole formation and evolution models

One of the targets of the new-LISA Parameter Estimation Taskforce is to assess the capabilities of a descoped LISA to detect supermassive black holes and measure their parameters. The cosmological evolution of massive black holes can be determined by merger tree simulations, following the merger history of dark matter halos and of the associated black holes by cosmological Monte Carlo realizations of the merger hierarchy from early times until the present in a  $\Lambda$ CDM cosmology with  $H_0 = 70 \text{ km s}^{-1} \text{ Mpc}^{-1}$ ,  $\Omega_M = 0.3$  and  $\Omega_\Lambda = 0.7$ . Merger tree simulations were used to produce ascii files listing the masses, redshifts and spins of merging black holes. The sample binaries used in the Taskforce are selected to assess the capabilities of LISA, not to allow for a reliable (and statistically significant) analysis of the black hole population.

Two important sources of uncertainty in merger tree models of black hole formation are (i) the formation mechanism and mass of the first "seed" black holes, and (ii) the details of how accretion causes black holes to grow in time (see [2] for more details). To bracket these uncertainties we focused on four representative models of massive black hole formation.

- **Seed masses.** As a representative model with "light" black hole seeds we considered the Volonteri-Haardt-Madau ([3], henceforth VHM) scenario, where light seed black holes of  $m_{\text{seed}} \sim \text{few times } 100 M_\odot$  are produced as remnants of metal-free stars at redshift  $z \gtrsim 20$ . Koushiappas, Bullock and Dekel suggested an alternative scenario where "heavy" seeds with  $m_{\text{seed}} \sim 10^5 M_\odot$  are formed as the end-product of dynamical instabilities arising in massive gaseous protogalactic disks in the redshift range  $10 \lesssim z \lesssim 15$  [4]. To allow for the possibility of heavy seeds, we considered a variant of this scenario proposed by Begelman, Volonteri and Rees ([5], henceforth BVR). Both models (VHM and BVR) can reproduce the AGN optical luminosity function in the redshift range  $1 \lesssim z \lesssim 6$ , but they result in very different coalescence rates of massive black hole binaries and hence in different gravitational wave backgrounds [2].

- **Spin evolution.** To bracket uncertainties in the evolution the black holes' *spin magnitude* due to accretion, we considered two different accretion models. We adopted either a "coherent accretion" scenario, where accretion of material with constant angular momentum axis rapidly spins up the holes [6, 7], or a "chaotic accretion" scenario [8], where accretion always proceeds via very small and short episodes (caused by fragmentation of the accretion disc where it becomes self-gravitating). Since counter-rotating material spins black holes down more efficiently than co-rotating material spins them up, and it is quite unlikely for mergers to produce rapidly spinning holes, this scenario implies that black hole spins are typically rather small [9]. The accretion prescription also leaves an imprint on the *mass growth* of black holes, and therefore on the masses of the two components at merger. The models assume that the mass-to-energy conversion efficiency,  $\epsilon$ , depends on black hole spin only, so the two models predict different average efficiencies of  $\sim 20\%$  and  $\sim 10\%$  respectively. The mass-to-energy conversion directly affects mass growth, with high efficiency implying slow growth, since for a black hole accreting at the Eddington rate, the black hole mass increases with time as

$$M(t) = M(0) \exp\left(\frac{1 - \epsilon}{\epsilon} \frac{t}{t_{\text{Edd}}}\right) \quad (19)$$

where  $t_{\text{Edd}} = 0.45 \text{ Gyr}$ . Therefore black holes in the SC and LC models are on average more massive than in the SE and LE models at a given cosmic time. The "coherent"

versus “chaotic” models thus allow us to study how different growth rates affect LISA observations. Finally, the assumed accretion prescription is likely to have an important effect on *spin alignment*. In gas-rich environments, the torque exerted by the gas is efficient in producing alignment of the black hole angular momenta with the (dominant) angular momentum of the circumbinary accretion disk (which has the same direction of the orbital angular momentum of the binary), as suggested in [10], and found in detailed SPH simulations by Dotti and collaborators [11] (see Ref. [9] for more details). If accretion proceeds in a chaotic fashion, there is no privileged direction for the spins of the black holes, and they can be assumed to be isotropically distributed.

- **Eccentricity.** We also include eccentricity in our models. Exactly circular massive black hole binaries are unlikely to exist in nature. Both gas driven and stellar driven binary evolution have been found to excite the eccentricity of the binary [12, 13, 14]. In the coherent accretion scenario, the massive circumbinary disk is likely to be also the dominant source of secular binary evolution. In this case, the binary is expected to achieve a limiting eccentricity of  $\sim 0.6$  [13], which is maintained through the inspiral until efficient gravitational wave emission takes over. The situation is less clear in the chaotic scenario. For the sake of comparison between different eccentricity evolution models, in this latter case we assume that the binary evolution is driven by stars. We employ the hybrid model proposed by [14] in which the binary evolves via scattering of bound and unbound stars in the galactic bulge. The process usually results in fairly high eccentricities. When the gravitational wave shrinking timescale is shorter than the gas/star driven binary migration, the binary decouples by its environment and circularizes. However, a significant amount of eccentricity can be retained at the moment it enters the frequency band relevant to gravitational wave observations, as shown in figure 17. It is worth mentioning that eccentricity evolution is implemented *a posteriori* on each individual binary, and it is not self consistently implemented in the merger trees.

*3.2.1. Details of the merger tree implementation* For each formation scenario, we usually have  $N_{\text{tree}} \sim 10$  different “merger trees” [15]. A merger tree traces the merger history that leads to a  $z = 0$  galaxy in a hierarchical cosmology. Each merger tree is characterized by a different mass of the parent halo at  $z = 0$  and by a different Press-Schechter weight  $W_{\text{PS}}^{(k)}$  ( $k = 1, \dots, N_{\text{tree}}$ ) [16, 17], which is used to scale the results to the (comoving) number density of sources. Furthermore, each merger tree has a different number  $N_{\text{real}}^{(k)}$  of realizations to take into account cosmic variance. Typically, large-mass halos have a smaller Press-Schechter weight (inherent in the adopted cosmological model) and a smaller number of realizations (due to computational burden).

For each tree  $k$  we have a list of black hole masses, spins and redshifts. All quantities in these files are measured in the source frame, at variance with the convention used in the Mock LISA Data Challenge (recall that  $M = (1 + z)M_{\text{source}}$ ). Each row in the list corresponds to “branches” of the tree where a merger event occurs. Including all merger trees and all realizations of each merger tree, in a typical model such as VHM we have at least  $\sim 5 \times 10^4$  merging events.

The number of events at a given redshift  $z$  per comoving volume is

$$N_{\text{com}}(z) = \sum_{k=1}^{N_{\text{tree}}} \sum_{j=1}^{N_{\text{mergers}}^{(k)}} \frac{W_{\text{PS}}^{(k)}}{N_{\text{real}}^{(k)}}, \quad (20)$$

The rate of potentially observable events at  $z = 0$  (note that no SNR cut has been performed in equation 20) per unit time and redshift is then given by Eq. (11) of Ref. [18] (see also [19]):

$$\frac{d^2 N}{dz dt} = 4\pi c N_{\text{com}}(z) [D_a(1+z)]^2 = 4\pi c N_{\text{com}}(z) D_c^2, \quad (21)$$

where  $D_c$  is the comoving distance and  $D_a$  is the angular diameter distance, both evaluated at redshift  $z$ .

*3.2.2. Detailed content of the files* To summarize, we have four black hole formation and evolution models, and we provide 5 catalogues of binary mergers. The first four catalogues are meant to be used for Model Selection (we follow the naming convention used by the first LISAPE taskforce), the fifth catalogue is to be used for the Horizon estimation. The models are labeled with different IDs (SE, SC, LE, LC, HOR), and each file name contains the ID of the reference models. The IDs are:

- **SE.** Small seeds, Efficient spin evolution. Model VHM, coherent accretion (aligned spins), gas driven dynamics (for eccentricity evolution);
- **SC.** Small seeds, Chaotic spin evolution. Model VHM, chaotic accretion (randomly oriented spins), star driven dynamics (for eccentricity evolution);
- **LE.** Large seeds, Efficient spin evolution. Model BVR, coherent accretion (aligned spins), gas driven dynamics (for eccentricity evolution);
- **LC.** Large seeds, Chaotic spin evolution. Model BVR, chaotic accretion (randomly oriented spins), star driven dynamics (for eccentricity evolution).
- **HOR:** an ‘average’ model, constructed by summing up the distributions  $d^3 N_i / dM_z dq dz$  (being  $M_z$  the total redshifted binary mass and  $q = M_2/M_1 < 1$  the binary mass ratio) and dividing by four. This model should be used for the ‘horizon determination’ of the new gravitational wave detector.

*Directory merger-trees* Here we collect the raw (before Press & Schechter weighting and comoving volume integration) merger tree outputs. There are 48 files **spins-merge-\*-model\***: 12 files (101-to-112) for each of the four models (SE-to-LC). Each file contains several realizations (20 for files 1-to-10, 10 for file 11, 5 for file 12) of a halo of a specific mass. The columns are as follows:

- 1-redshift
- 2-3-nevermind
- 4- $M_1$  (in the source frame)
- 5-mass ratio,  $q = M_2/M_1 \leq 1$
- 6-normalized spin magnitude of black hole 1,  $a_1$
- 7-normalized spin magnitude of black hole 2,  $a_2$
- 8-nevermind

The file **PS-J.dat** contains the twelve Press & Schechter weights (1-to-12 from the top to the bottom).

*Directory distributions* Here we collect the relevant binned distributions of each model. The files **model\*-DNzmq.OUT** contain the trivariate distributions  $\Delta^3 N / (\Delta z \Delta M_z \Delta q)$  evaluated on a grid in  $(z, M_z, q)$ . If desired, any new Montecarlo realization of the black hole population can be extracted directly from these files. In all the files located in this directory, grids are as follow:

- The  $z$  interval  $[0, 20]$  is divided in 20 intervals. of width  $\Delta z = 1$  in the range.
- The  $\log M_z$  interval  $[1, 11]$  is divided in 40 equally spaced log bins.
- The  $\log q$  interval  $[-5, 0]$  is divided in 30 equally spaced log bins.
- The  $a$  interval  $[0, 0.998]$  is divided in 100 equally spaced bins.

The columns are as follows.

(i) Files **model\*-DNzmq.OUT**

- column 1-lower bound of the  $z$  bin
- column 2-lower bound of the  $M_z$  bin
- column 3-lower bound of the  $q$  bin
- column 4- $\Delta^3 N / (\Delta z \Delta M_z \Delta q)$ , events predicted by the models

These distributions are normalized so that the sum over all the bins is equal to  $N_{3\text{yr}}$  (i.e.  $\sum_{\Delta z} \sum_{\Delta M_z} \sum_{\Delta q} \Delta^3 N / (\Delta z \Delta M_z \Delta q) = N_{3\text{yr}}$ ), i.e. the total number of events predicted by the model in a three year observation (240 for model SE; 227 for model SC; 72 for model LE; 67 for model LC; 151 for model HOR).

(ii) Files **model\*-DNz.OUT**:

- column 1-lower bound of the  $z$  bin
- column 2-upper bound of the  $z$  bin
- column 3- $\Delta N / \Delta z$ , total events predicted by the model

(iii) Files **model\*-DNm.OUT**:

- column 1-lower bound of the log of the  $M_z$  bin
- column 2-upper bound of the log of the  $M_z$  bin
- column 3- $\Delta N / \Delta M_z$ , events predicted by the models

(iv) Files **model\*-DNq.OUT**:

- column 1-lower bound of the log of the  $q$  bin
- column 2-upper bound of the log of the  $q$  bin
- column 3- $\Delta N / \Delta q$ , events predicted by the models

(v) Files **model\*-DNa1a2.OUT**:

- column 1-lower bound of the spin bin
- column 2-upper bound of the spin bin
- column 3- $\Delta N / \Delta a_1$ , for the primary black hole
- column 4- $\Delta N / \Delta a_2$ , for the secondary black hole

Files (ii-v) contain differential distributions normalized to  $\sum_{\Delta X} (\Delta N / \Delta X) \Delta X = N_{3\text{yr}}$ , where  $X$  is either  $z$ ,  $M_z$ ,  $q$ ,  $a_1$ ,  $a_2$ . These distributions are useful to compare marginal distributions as shown in figures 16 and 17.

N.B. There is no spin distribution for model HOR. For horizon studies, we suggest to assume two extreme cases for the spins:

- 1-no spin
- 2- $a_1 = a_2 = 0.9$ , aligned to the binary angular momentum.

*Directory Montecarlo catalogues* In this directory we place the files **model\*-MCEvents.OUT**, containing the Montecarlo catalogues to be used for parameter estimation, model selection study, etc. There are 10 realizations for models SE, SC, LE,LC and 100 realizations for model HOR, to provide better statistics for horizon determination studies, if desired. A file containing only the first realization of the HOR model (model-HOR-MCEvents-test.OUT, 140 coalescences) is provided as a reference for all groups to run the basic horizon studies.

The number of sources in each realization is drawn by a Poissonian distribution with a mean given by  $N_{3\text{yr}}$  (240 for model SE; 227 for model SC; 72 for model LE; 67 for model LC; 151 for model HOR). Columns are as follows:

- column 1-realization ID
- column 2-source ID
- column 3-source redshift
- column 4- $M_1$  (restframe) in solar masses
- column 5-mass ratio  $q$
- column 6-ecliptic longitude,  $\phi_s$  (random in the interval  $[0, 2\pi]$ )
- column 7-ecliptic latitude,  $\theta_s$  (in the interval  $[-\pi/2, \pi/2]$ , sampled with probability  $\cos(\theta_s + \pi/2)$ )
- column 8-azimuthal direction of the binary orbital angular momentum  $L$ ,  $\phi_L$  (random in the interval  $[0, 2\pi]$ )
- column 9-polar direction of the binary orbital angular momentum  $L$ ,  $\theta_L$  (in the interval  $[0, \pi]$ , sampled with probability  $\cos\theta_L$ )
- column 10-initial phase,  $\phi$  (random in the interval  $[0, 2\pi]$ )
- column 11-coalescence time  $t_c$  in seconds (random in the interval  $[0, 3\text{yr}]$ )
- column 12-magnitude of spin 1
- column 13-magnitude of spin 2
- column 14-polar direction of spin 1,  $\theta_{a_1}$  (in the interval  $[0, \pi]$ , sampled with probability  $\cos\theta_{a_1}$  for chaotic models;  $= 0$  for coherent models)
- column 15-polar direction of spin 2,  $\theta_{a_2}$  (in the interval  $[0, \pi]$ , sampled with probability  $\cos\theta_{a_2}$  for chaotic models (SC,LC);  $= 0$  for coherent models (SE, LE))
- column 16-azimuthal direction of of spin 1,  $\phi_{a_1}$  (random in the interval  $[0, 2\pi]$  for chaotic models (SC,LC);  $= 0$  for coherent models (SE,LE))
- column 17-6-azimuthal direction of of spin 2,  $\phi_{a_2}$  (random in the interval  $[0, 2\pi]$  for chaotic models (SC,LC);  $= 0$  for coherent models (SE,LE))
- column 18-azimuthal direction of the binary pericenter,  $\gamma$  (random in the interval  $[0, 2\pi]$ )
- column 19-residual eccentricity at an *observed* gravitational wave frequency of  $10^{-4}$  Hz. Where the gravitational wave frequency is intended to be the frequency of the second harmonic (i.e. twice the orbital *redshifted* frequency)

The binary lies in the  $x - y$  plane of the  $(x, y, z)$  reference frame centered in its center of mass, with orbital angular momentum  $L$  initially pointing in the  $z$  direction. The angles defining the individual binary spins ( $\theta_{a_1}$ ,  $\phi_{a_1}$ ,  $\theta_{a_2}$ ,  $\phi_{a_2}$ ) the binary phase ( $\phi$ ) and the direction of the initial binary periastron ( $\gamma$ ) are measured in this frame, with azimuthal angles measured counterclockwise starting from the  $x$  axis. The  $x$  axis points from the source toward the Earth. The angles defining the direction of the binary angular momentum  $L$  ( $\theta_L$ ,  $\phi_L$ , i.e. the orientation of the binary plane) and

the sky location  $(\theta_s, \phi_s)$ , are measured in the ecliptic frame  $(x_e, y_e, z_e)$ . Additional script (can be found on the wiki) was used to translate spin angles from source frame to ecliptic frame. Those together with estimations of the luminosity distance, chirp mass and symmetric mass ratio were added as extra columns.

N.B. For model HOR, only the first 11 columns are present. We consider the binaries to be circular in this case. As stated before, for horizon studies, we suggest to assume two extreme cases of (i) non spinning binaries, and (ii) binaries with  $a_1 = a_2 = 0.9$ , aligned to the binary angular momentum.

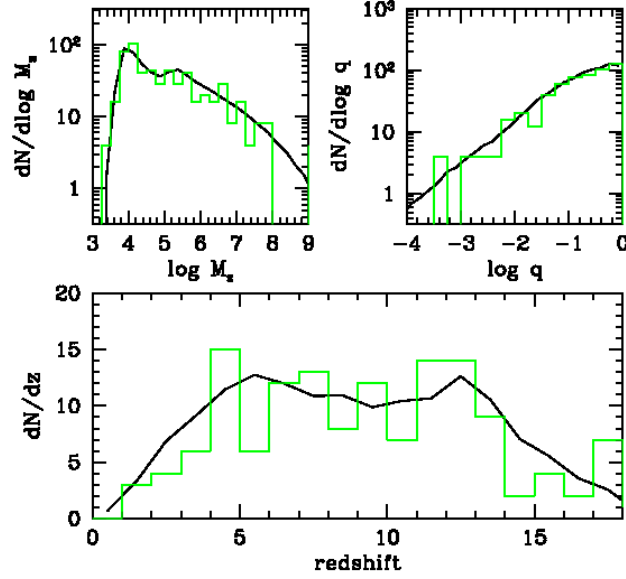


Figure 15: Example of marginalized  $dN/dM_z$  (upper left panel),  $dN/dq$  (upper right panel) and  $dN/dz$  (lower panel) distributions for model HOR. In each panel, the black lines are the marginalized distributions contained in the files located in the directory 'distributions'. The green histograms are the distributions obtained by realization 1 in the file model-HOR-MCevents.OUT in the 'montecarlo-catalogues' directory.

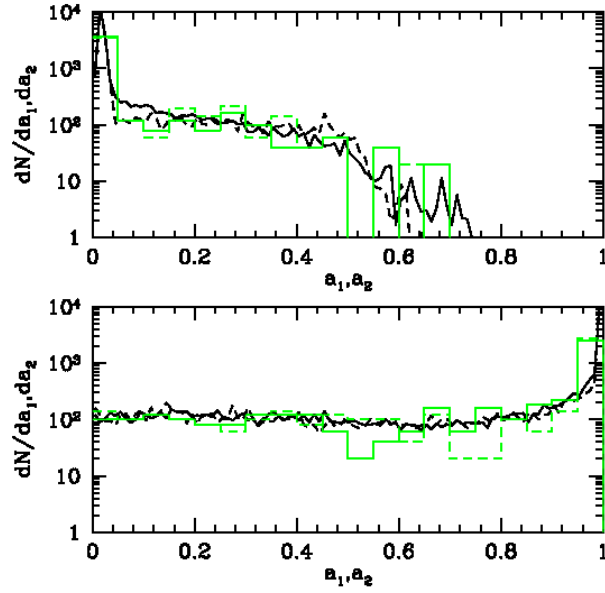


Figure 16: Example of marginalized spin distributions  $dN/da_1$  (solid lines) and  $dN/da_2$  (dashed lines) for models SE (VHM coherent, lower panel) and SC (VHM chaotic, upper panel). Histograms are the distributions obtained by realization 1 in the file model-SC-MCevents.OUT (upper panel) and model-SE-MCevents.OUT (lower panel) in the 'montecarlo-catalogues' directory.

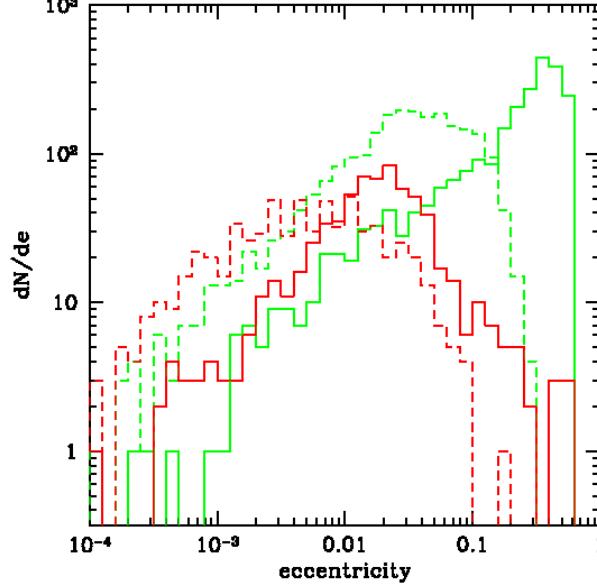


Figure 17: Eccentricity distributions at *observed* gravitational wave frequency of  $10^{-4}$  Hz for model SE (VHM coherent, solid green histogram), SC (VHM chaotic, dashed green histogram), LE (BVR coherent, solid red histogram), LC (BVR chaotic, dashed red histogram). Coherent models are evolved via gas dynamics, whereas star driven dynamics is assumed for the chaotic models. The distributions are obtained by averaging over the 10 Montecarlo realizations contained in the respective model\*-MEvents.OUT files in the 'montecarlo-catalogues' directory.

### 3.3. Parameter estimation

(*'section captains'* : Neil Cornish & Emanuele Berti)

**3.3.1. Averaged SNRs and horizon distances** (Emanuele Berti, Neil Cornish, & Stas Babak) Let us consider the restricted PN waveforms as computed (say) in Maggiore's book:

$$\tilde{h}(f) = \sqrt{\frac{5}{6}} \frac{\mathcal{M}^{5/6} f^{-7/6}}{2\pi^{2/3} D_L} e^{i\psi} \frac{2Q}{2}. \quad (22)$$

where we write  $Q = 2Q/2$  for reasons that will be apparent below. Here

$$Q = \frac{1 + \cos^2 \iota}{2} F_+ + i \cos \iota F_\times. \quad (23)$$

The angular average of the modulus squared of  $2Q$  yields

$$\langle (1 + \cos^2 \iota)^2 F_+^2 + 4 \cos^2 \iota F_\times^2 \rangle^{1/2} = \frac{4}{5}, \quad (24)$$

so we get an angle-averaged Fourier amplitude of

$$\tilde{h}(f) = \sqrt{\frac{5}{6}} \frac{\mathcal{M}^{5/6} f^{-7/6}}{2\pi^{2/3} D_L} e^{i\psi} \frac{2}{5} = \frac{1}{\sqrt{30}} \frac{\mathcal{M}^{5/6} f^{-7/6}}{\pi^{2/3} D_L} e^{i\psi}. \quad (25)$$



which is the same as Eq. (2.1b) in [20]. We multiply this by  $\frac{\sqrt{3}}{2}$  to take into account the  $60^\circ$  orientation of the LISA configuration, so our starting point is Eq. (2.1a) in [20]:

$$\tilde{h}(f) = \frac{\sqrt{3}}{2} \frac{1}{\sqrt{30}} \frac{\mathcal{M}^{5/6} f^{-7/6}}{\pi^{2/3} D_L} e^{i\psi}. \quad (26)$$

The SNR is defined in the usual way (see e.g. Eq. (2.6) in [20]):

$$\rho^2 = 4 \int_{f_{\text{in}}}^{f_{\text{fin}}} \frac{|\tilde{h}(f)|^2}{S_n^{\text{NSA}}(f)} df, \quad (27)$$

where the *non sky-averaged* noise spectral density  $S_n^{\text{NSA}}(f)$  is related to the *sky-averaged* (but not inclination-averaged!) noise spectral density provided by Neil and by Shane's Sensitivity Curve Generator,  $S_n^{\text{SA}}(f)$ , by

$$S_n^{\text{NSA}}(f) = \frac{3}{20} S_n^{\text{SA}}(f). \quad (28)$$

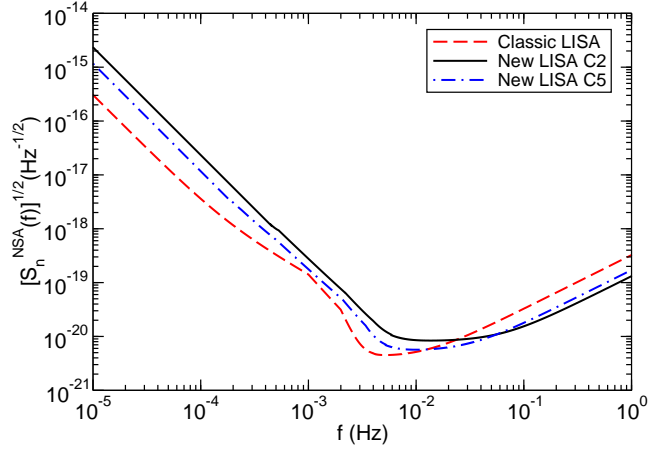


Figure 18: Non-sky averaged noise spectral density, Eq. (28), for Classic LISA and for New LISA C2/C5 including the galactic background.

Putting everything together, the integral to compute for restricted PN inspirals is

$$\rho = \sqrt{\frac{2}{3}} \frac{\mathcal{M}^{5/6}}{\pi^{2/3} D_L} \left[ \int_{f_{\text{in}}}^{f_{\text{fin}}} \frac{f^{-7/3}}{S_n^{\text{SA}}(f)} df \right]^{1/2}. \quad (29)$$

The SNR for phenomenological waveforms is computed following the same conventions. For the 5/6 link configurations, these average SNRs are then multiplied by a factor  $\sqrt{2}$ . In the present calculation we use the PHENOMC model [21], but if needed for comparisons we can easily compute SNRs for PHENOMA [22] and PHENOMB [23].

Horizon distances are computed as follows: for a given cosmological model (here  $\Omega_M = 0.28$ ,  $\Omega_\Lambda = 0.72$ ,  $H_0 = 70$  km/s/Mpc), first compute the SNR as a function of  $M_z = M(1+z)$  at (say)  $z = 1$ . Then use the fact that  $\text{SNR} \sim D_L^{-1}$  to find the horizon luminosity distance  $D_{L,\text{hor}}$  at which  $\text{SNR} = 10$ . Finally, find the redshift  $z_{\text{hor}}(D_{L,\text{hor}})$

corresponding to that luminosity distance by inverting (numerically)  $D_L(z)$ . Horizon distances and redshifts are plotted as functions of the mass  $M$  in the *source* frame.

The right panel of Fig. 20 shows that, even including merger and ringdown, Configuration 2 is necessary to reach  $z > 10$  for all  $M \gtrsim 10^4 M_\odot$ .

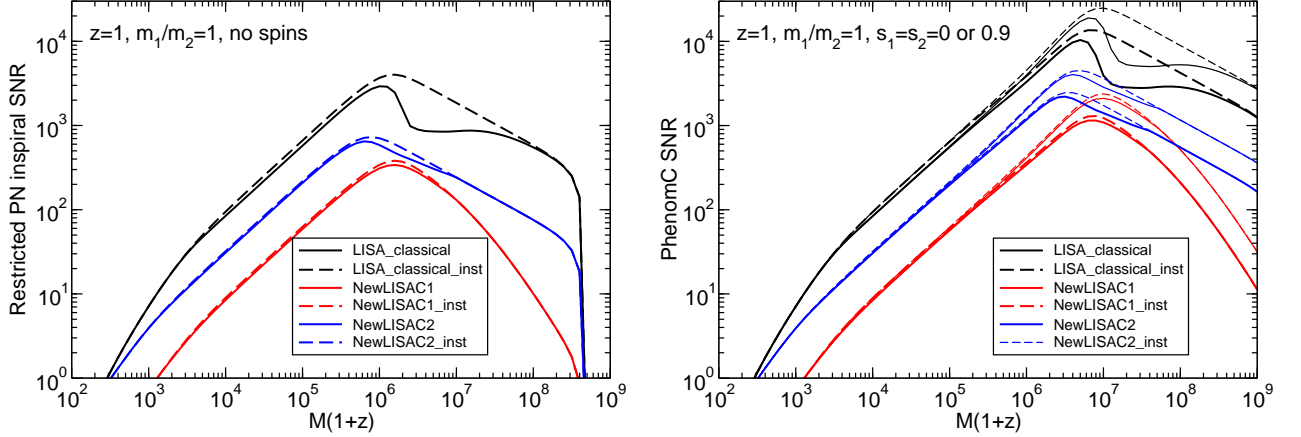


Figure 19: Angle-averaged SNR for equal-mass, nonspinning binaries as a function of redshifted mass,  $M_z = M(1+z)$ . Solid lines: instrumental noise+galactic background; dashed lines: instrumental noise only. Left: restricted PN inspiral; right: PHENOMC inspiral/merger/ringdown. In the right panel, thick lines refer to nonspinning binaries, and thin lines refer to binaries with  $s_1 = s_2 = 0.9$ . **EB: If we decide to keep this and the following plots, I should replace C1 by C5.**

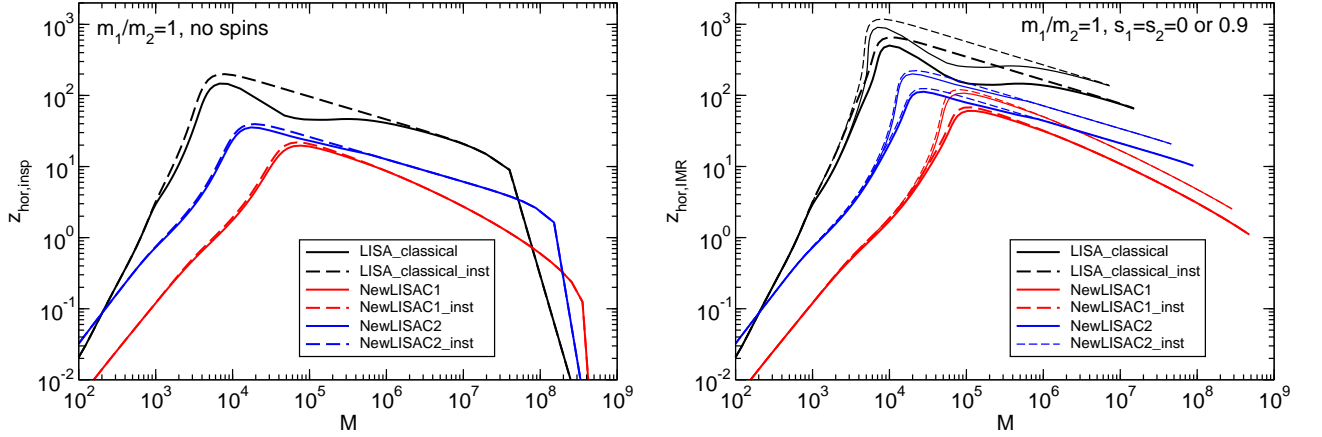


Figure 20: Horizon redshift  $z_{\text{hor}}$  (in Mpc) for equal-mass binaries as a function of the source mass  $M$ . Left: restricted PN inspiral; right: PHENOMC inspiral/merger/ringdown. Linestyles are the same as in Fig. 19.

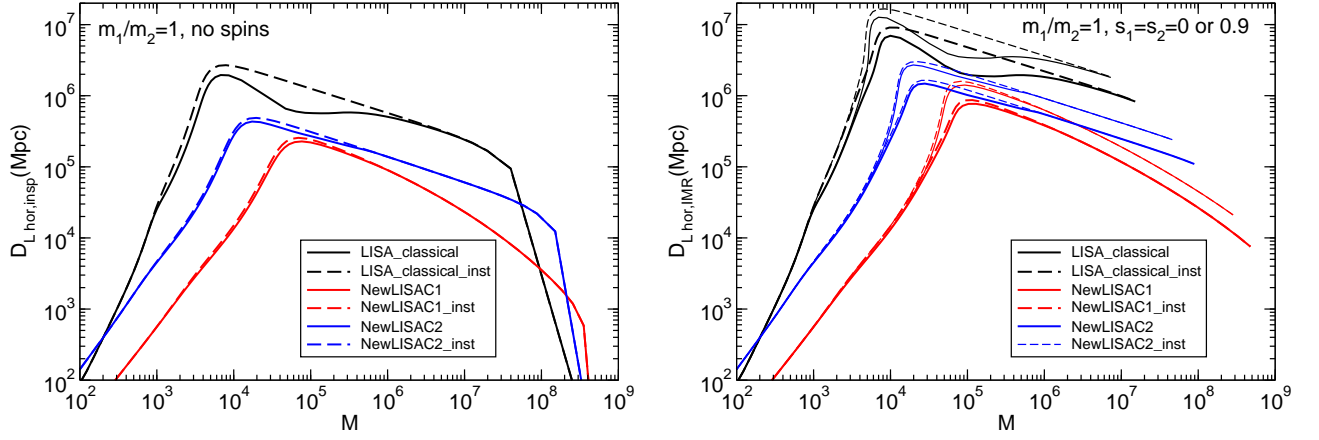


Figure 21: Horizon luminosity distance  $D_{L,\text{hor}}$  (in Mpc) for equal-mass binaries as a function of the source mass  $M$ . Left: restricted PN inspiral; right: PHENOMC inspiral/merger/ringdown. Linestyles are the same as in Fig. 19.

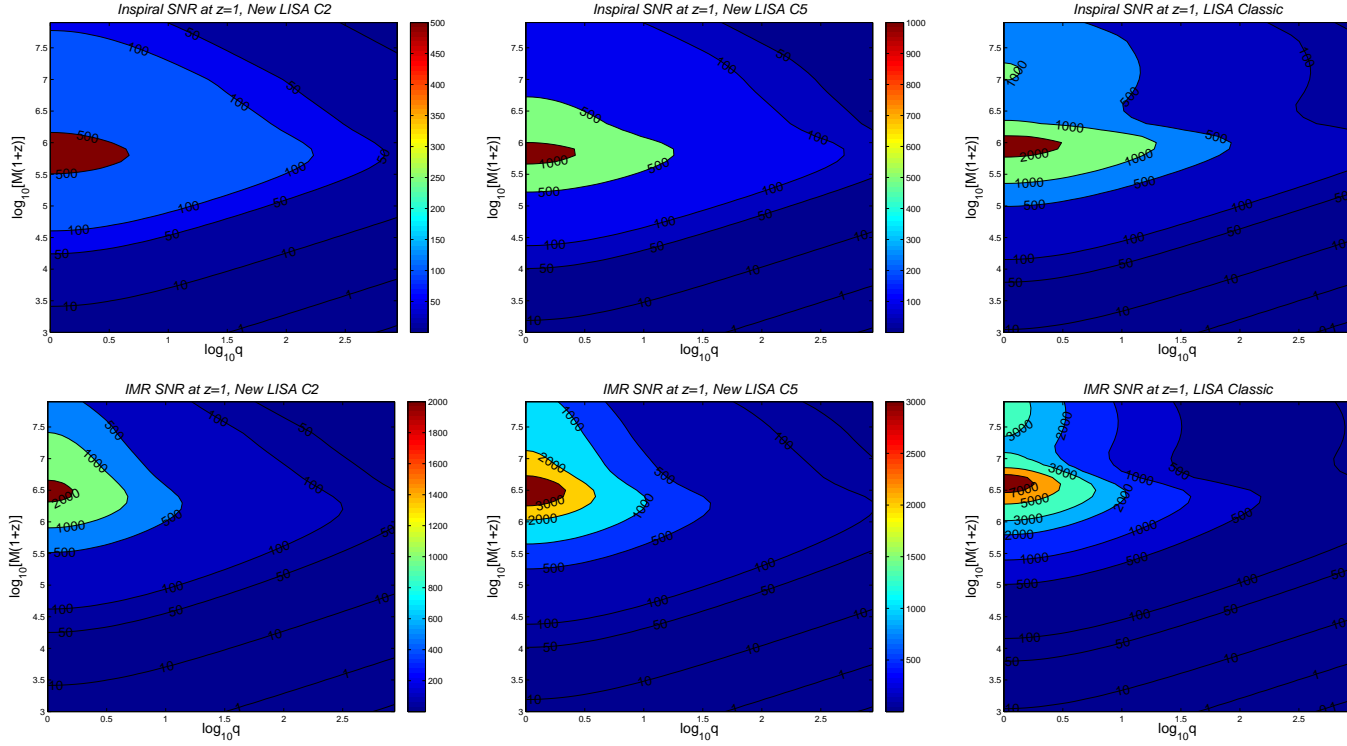


Figure 22: Angle-averaged SNR for equal-mass, nonspinning binaries at  $z = 1$ .

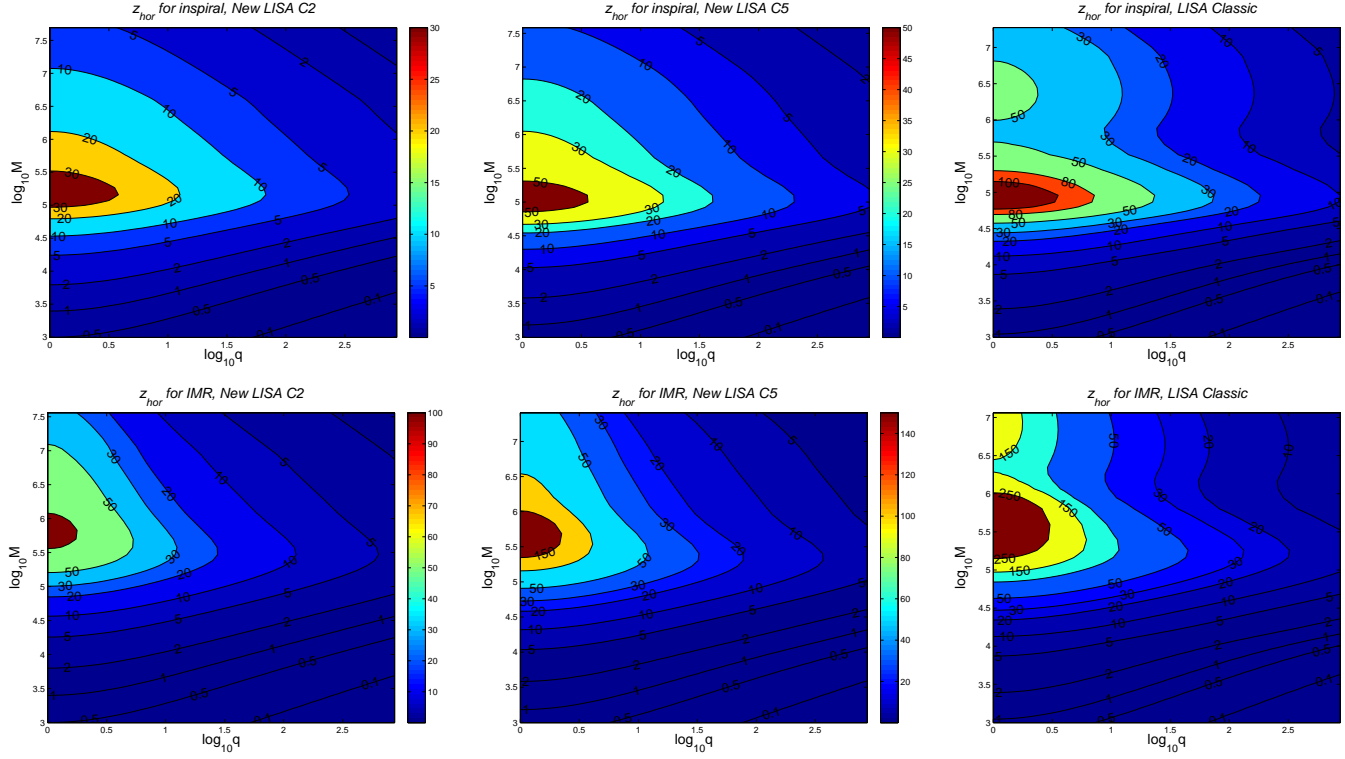
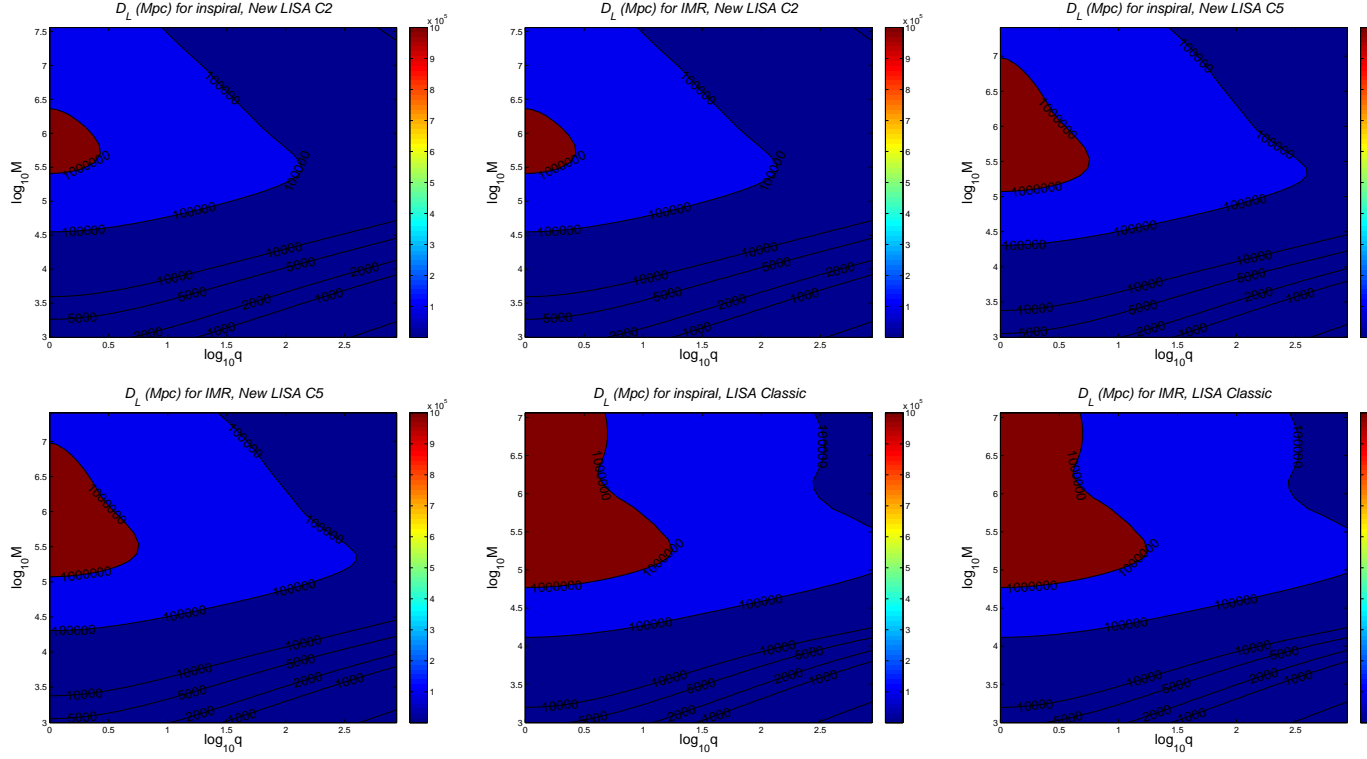
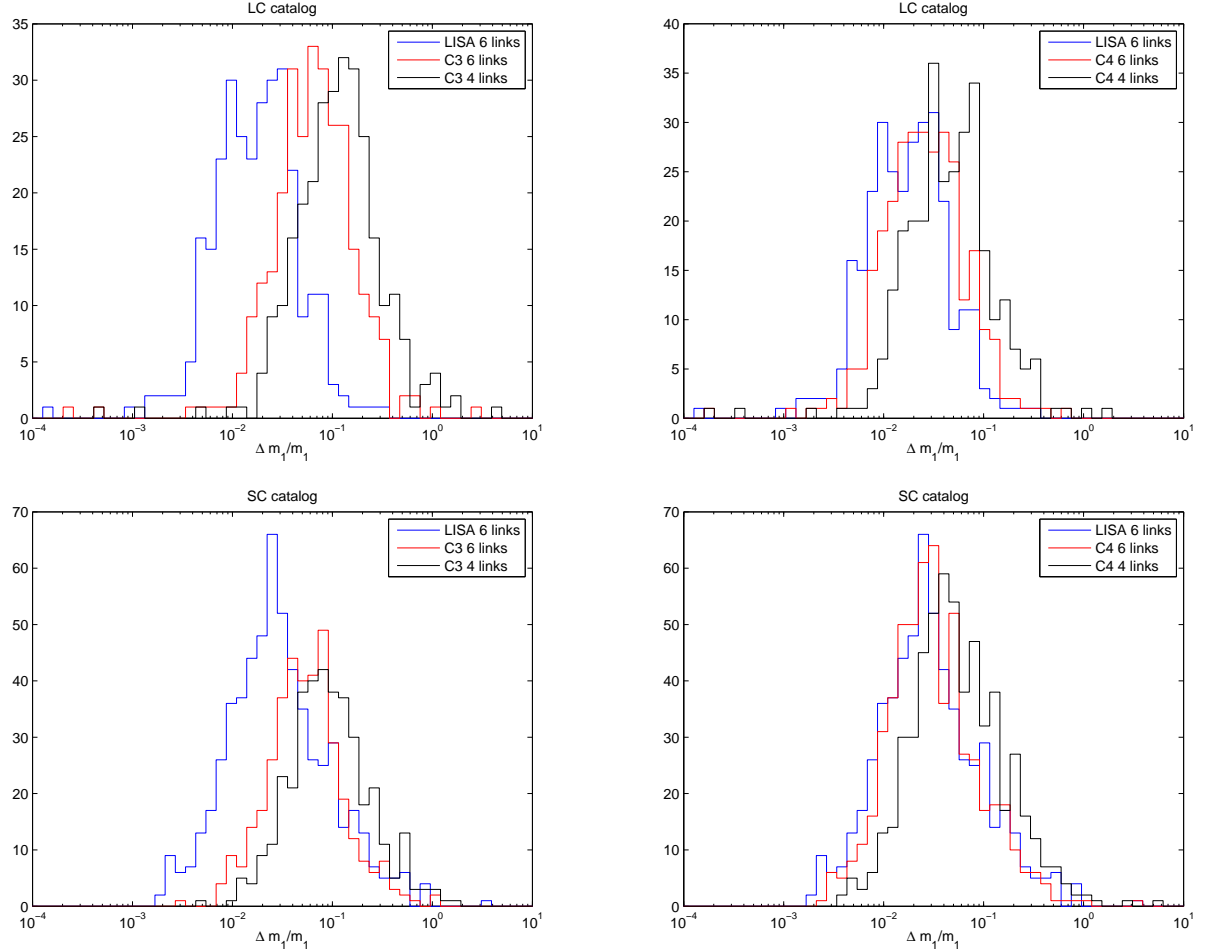


Figure 23: Horizon redshift.

*3.3.2. Results using inspiral waveform with spin precession and higher harmonics (Ryan Lang & Neil Cornish)* Preliminary results for parameter estimation with spin precession and higher harmonics Sources: LC and SC catalogs, requiring  $\text{SNR} > 8$  (6 link case),  $3 \text{ months} < t_c < 2 \text{ years}$ , mass ratio  $< 50$ . (SCClassic and SCConfig4 are not quite done but have more viable sources than the other cases.)

Figure 24: Horizon (luminosity) distance  $D_L$ .

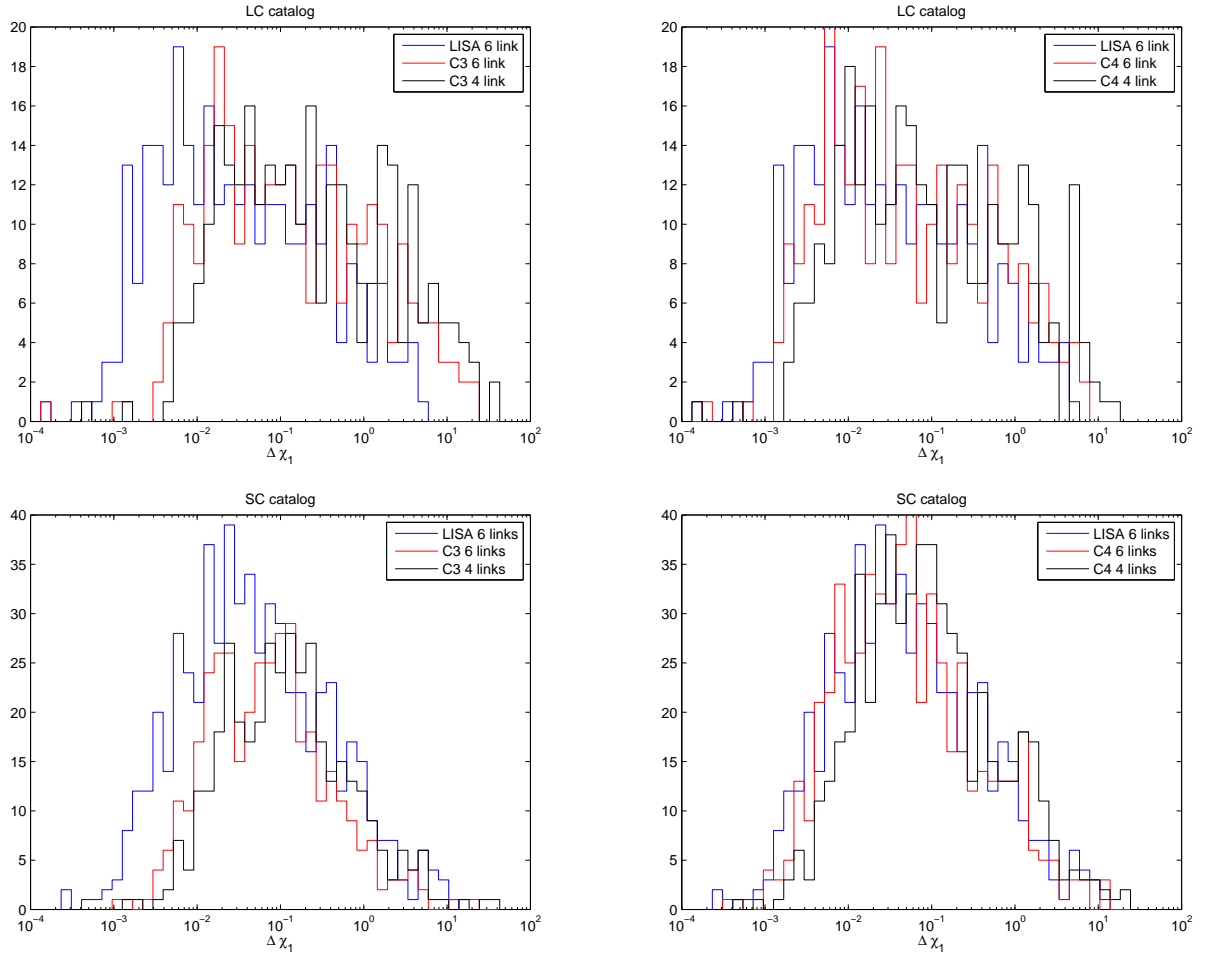


Figure 26: Spin error

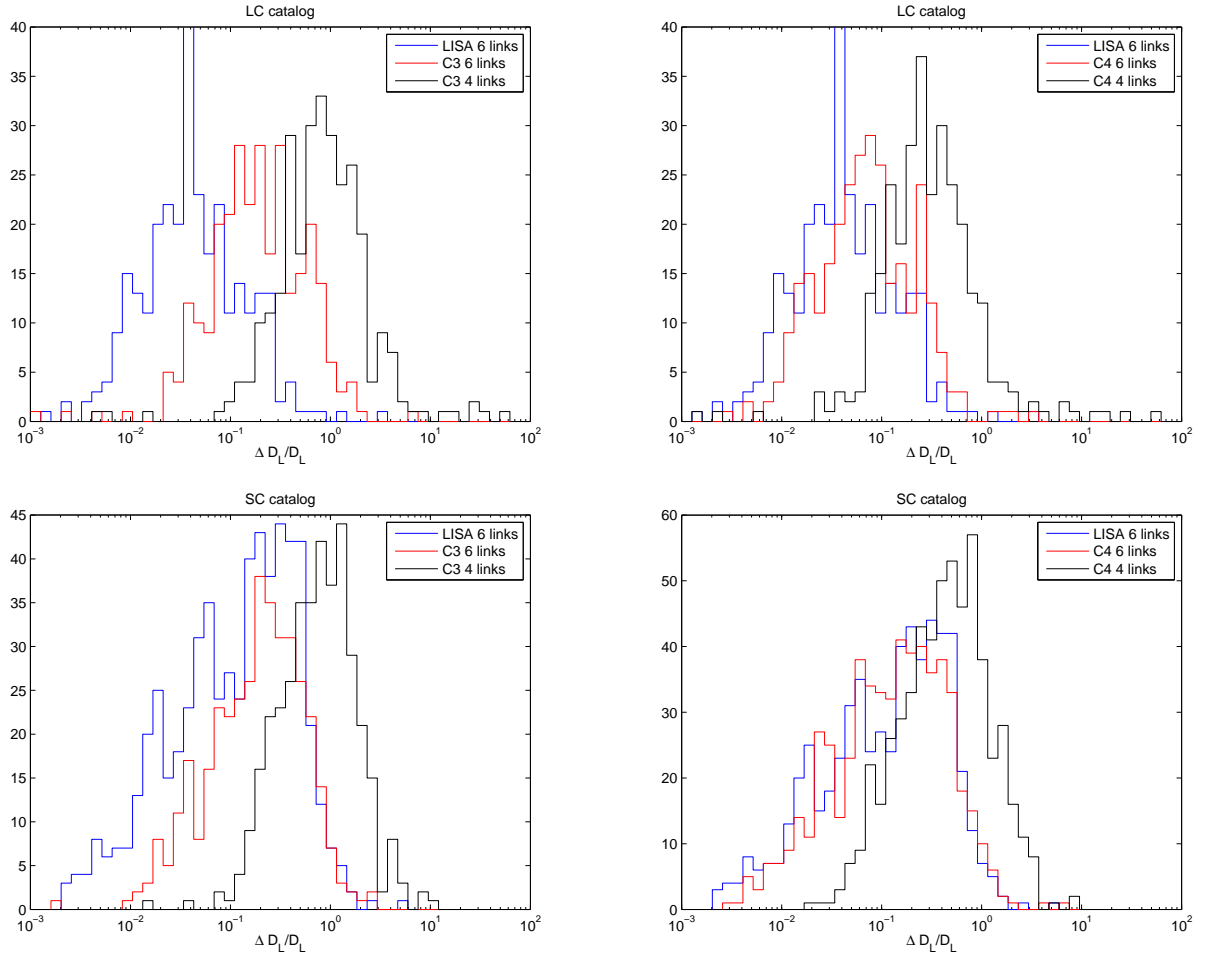


Figure 27: Distance error

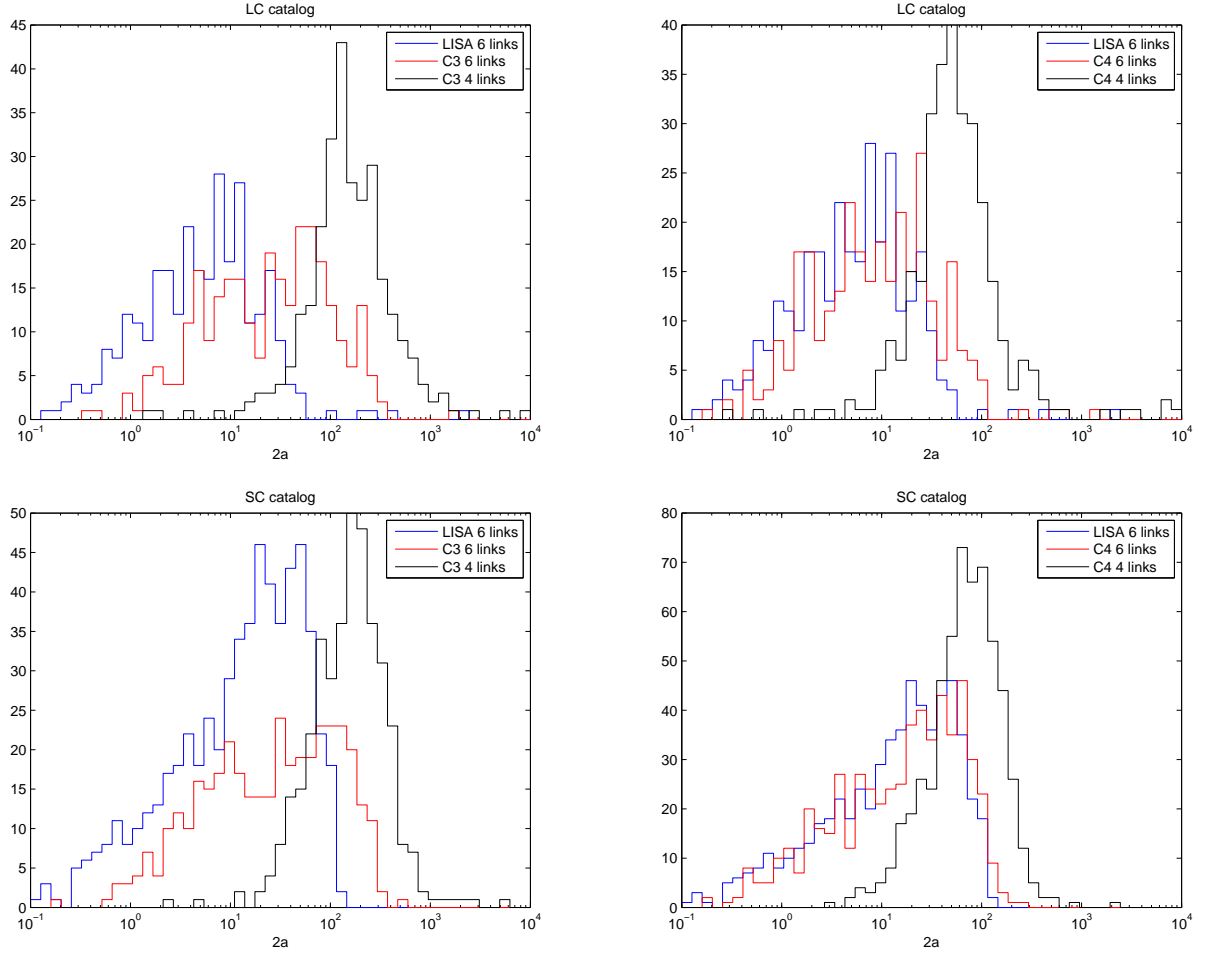


Figure 28: Sky position major axis (degrees)

### 3.3.3. Results using inspiral waveform with spin precession and higher harmonics (Antoine Petiteau, Sofiane Aoudia & Stas Babak)

**3.3.4. Inspiral-Merger-Ringdown with higher harmonics (EOB based) (Sean McWilliams)** We focus specifically on configuration 5, although we expect our conclusions will apply more generally. We performed a Fisher analysis on the aligned spin catalogs, using a waveform model that includes all available post-Newtonian corrections to the inspiral phase and amplitude, as well as a merger model which includes all relevant harmonic content. We do not include spin precession, so the relative amount of improvement due to higher harmonics (HHs) in the merger should be considered an upper limit. The uncertainty itself should also be considered an upper limit, meaning we expect that precession will generically make parameter uncertainties smaller despite the introduction of 4 extra parameters.

We can draw several conclusions from the uncertainty histograms. First, we note that our 4 link results without HHs should be comparable to the results using



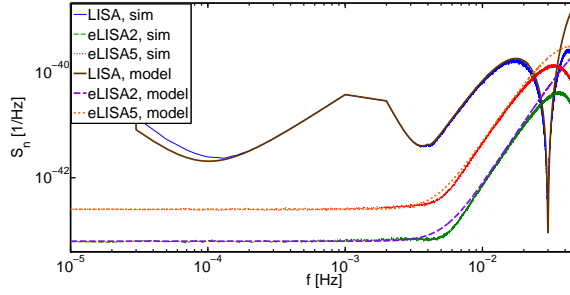


Figure 29: Comparison of noise model with average of a 1000-case ensemble of noise realizations using SYNTHETIC LISA, for the  $A$  channel with classic LISA and configurations 2 and 5.

PhenomC mergers, which also lack HHs. It is interesting that HHs have as large an impact in log space as going from 4 to 6 links does for the distance determination, for both large and small seed catalogs. This seems to be due primarily to the determination of  $\iota$ , which is the same with 4 links and HHs as it is for 6 links with HHs. Since the majority of the benefit from HHs comes from the very late inspiral and merger, we expect the improvement in distance determination we see to be more dramatic than results that include HHs in the inspiral, but not the merger. Codes with precession and HHs in the inspiral but not in the merger will see even less importance from HHs, as precession may break the same degeneracies that we see broken by HHs. We also see significant improvement in sky localization, with HHs improving latitude and longitude uncertainties by half an order of magnitude. However, this is much less than the improvement one would expect from 6 links, which yields an additional order-of-magnitude improvement beyond the inclusion of HHs. All angle parameters show improvement from HHs, as does the mass ratio, but the uncertainty in spin magnitude is unaffected by either HHs or 6 links.

### 3.3.5. Results using inspiral waveform with higher harmonics (Ed Porter)

### 3.3.6. Results using ringdown phase (Ioannis Kamaretsos, B.Sathyaprakash)

3.3.7. Results using PhenomC (Inspiral-Merger-Ringdown) from AEI (Stas Babak, Antoine Petiteau, Alberto Sesana, Frank Ohme & Emma Robinson) We use PhenomC waveforms described in [21]. Waveforms include merger and ringdown and assume aligned spins. Given the latter assumption, we apply them to efficient accretion models (SE, LE) only. Moreover, since the waveforms can not handle too extreme cases, we lower the maximal spin limit to 0.98, and considered only sources with mass ratio larger than  $q = M_2/M_1 = 0.05$ , thus losing 10-20% of the sources (depending on the MBH population model) in our analysis. The waveform is designed only for a dominant (2,2) harmonic and  $h_+, h_x$  are generated in the frequency domain. We have used rigid-adiabatic approximation to the TDI response (1st generation). For the

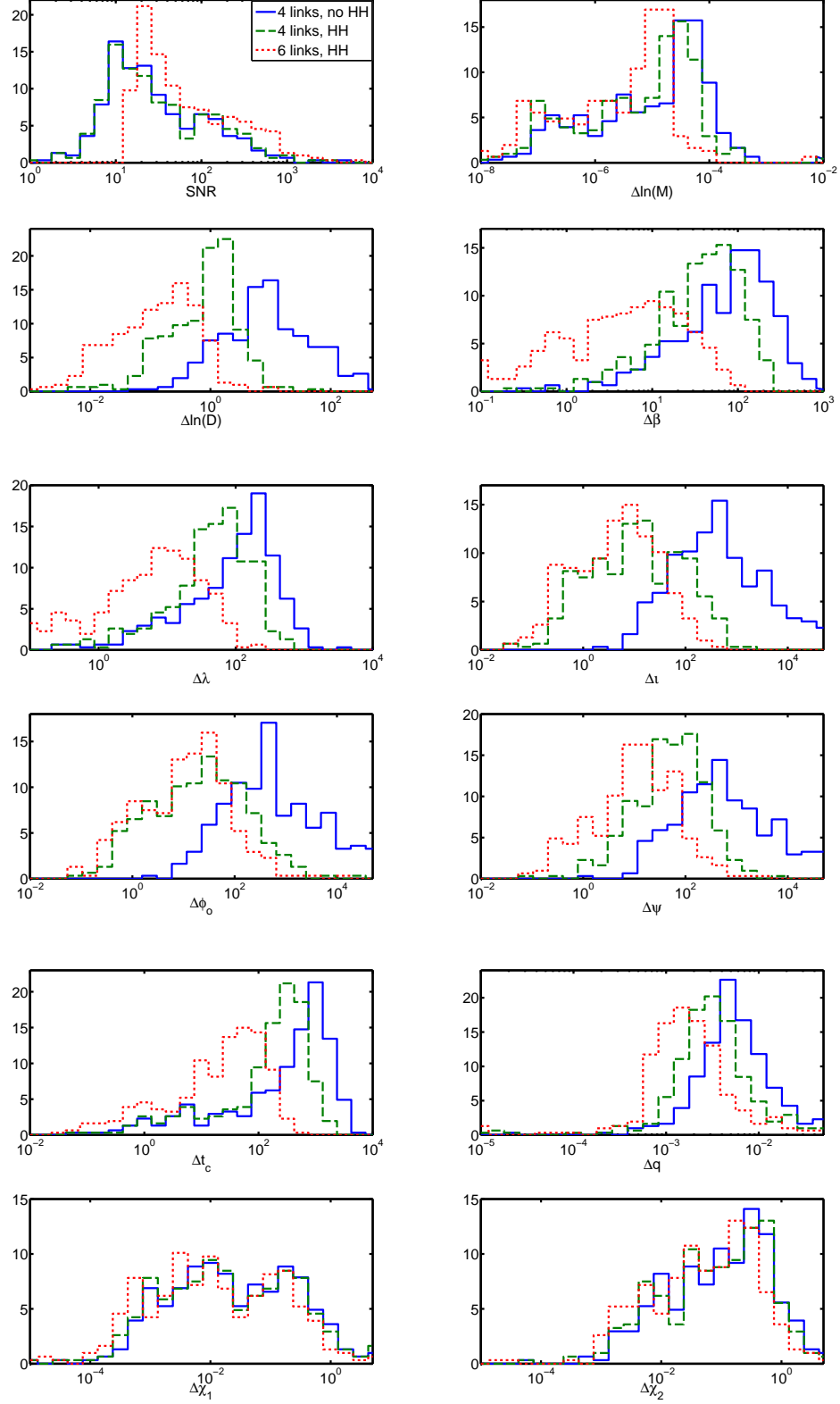


Figure 30: Uncertainty histograms for the large seed, aligned spin catalog, using the configuration 5 LISA redesign. All angle uncertainties are in degrees,  $\Delta t_c$  is in seconds, and mass and distance errors are fractional. The catalog spin values are not used, but rather all cases are given dimensionless spins  $\chi_{1,2} = S_{1,2}/M_{1,2}^2 = 0.5$  due to the limitations of our model for HHs.

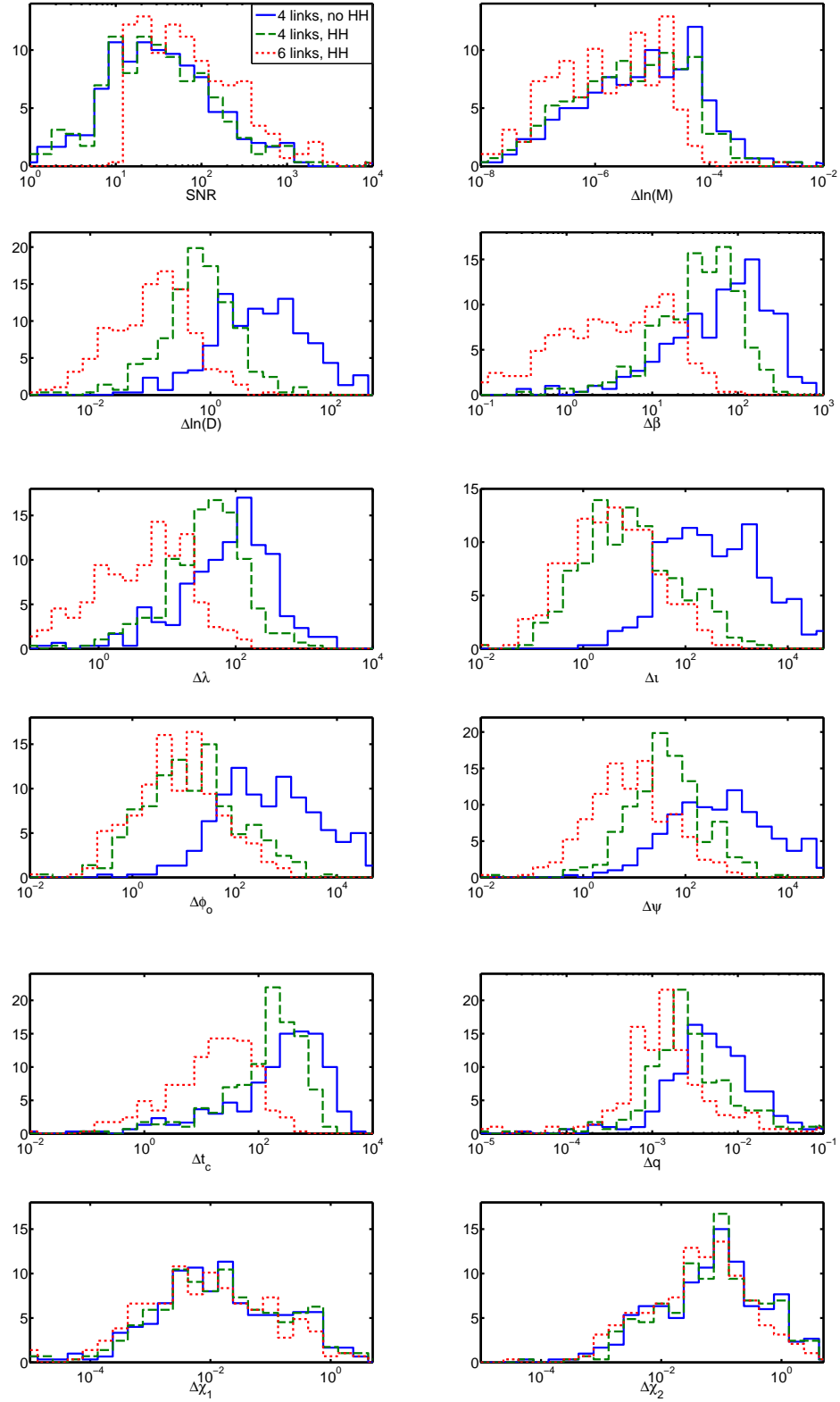


Figure 31: Uncertainty histograms for the small seed, aligned spin catalog using configuration 5.

inspiral part we have considered the spacecraft motion by using the correspondence (via stationary phase approximation) between frequency of the GW signal and the time. However this relationship becomes not applicable as we approach the merger (we use monotonous increase in time and in frequency as validity condition). For the merger and the ringdown (less than few days) we have assumed the static LISA. This simplified assumption does not affect SNR estimation but might overestimate (slightly) the error for the sky location. Some information about the sky location comes from the triangulation (at high frequency) as GW signal propagates across the constellation, and other information is due to modulation of the amplitude through antenna pattern and Doppler modulation of the phase. Assumption of the static LISA removes the modulation of the signal. For the halo orbit around L1 we have used the numerical orbit and assuming adiabatic evolution of the GW signal.

We consider a threshold  $\text{SNR} = 6$  for detection, and  $\text{SNR} = 10$  for trustworthy parameter estimations. We show results for detectors LISA, halo L1, C4, C5, C2, C3 and C5, assuming a single Michelson interferometer.

First we consider the detection abilities of different configurations for that we have considered all realizations and sources from the “**HOR**” catalog described earlier in the section 3.1. The LISA and C2 configurations are given in the figures 32, 33 below. In all these figures the horizontal axis is the redshift. The top panel shows the average SNR for a given configuration (black circles) upper and lower triangles show the dispersion (one sigma). The second panel from the top gives an average over realizations fraction of the detected events with one sigma error bar. This plot has to be read together with the lower panel which gives the average number of detectable events (third panel from the top). The last (bottom) panel gives the accumulative number of the detected events with the legend providing the average number of the events observed up to redshift 5 and the total.

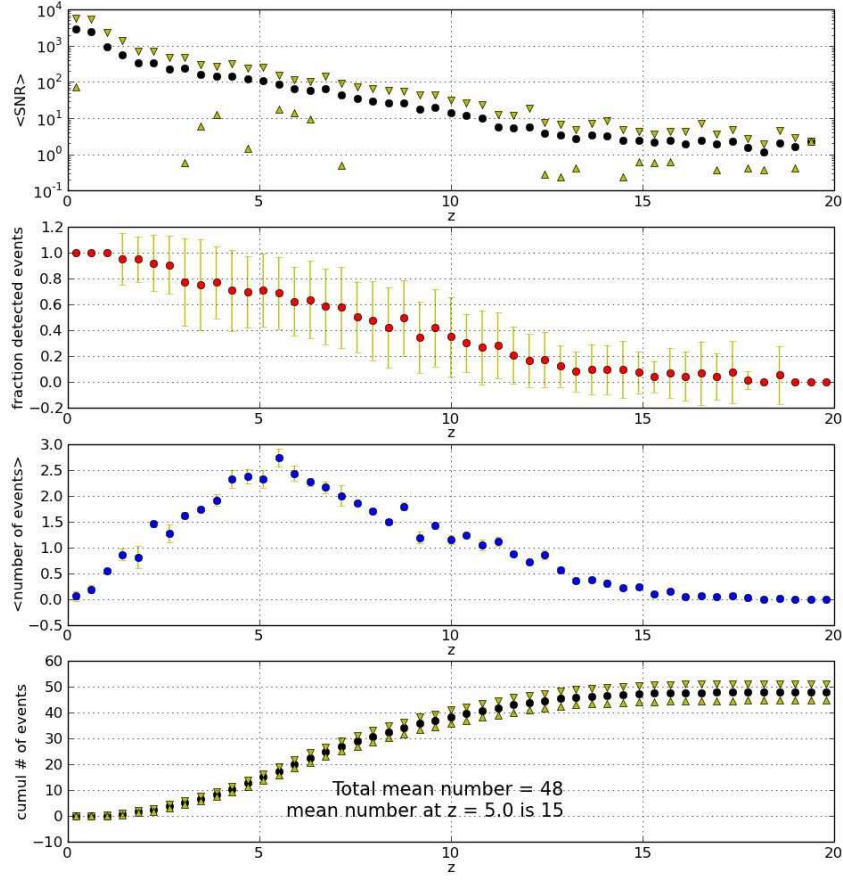


Figure 32: LISA performances as a function of redshift. From the top to the bottom we plot the average source SNR, the fraction of detectable sources ( $\text{SNR} > 6$ ), the mean number of detected sources, and the cumulative number of detected sources. Error bars are standard deviations; SE population model is assumed.

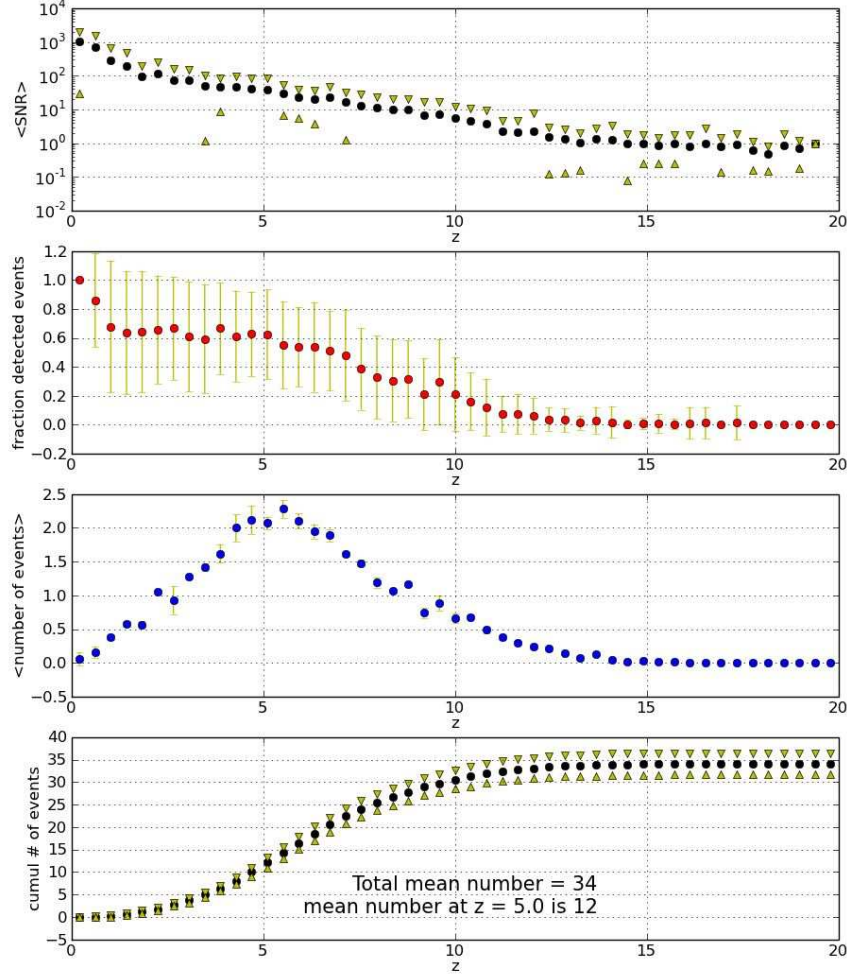


Figure 33: Same as figure 32 but for C2.

The next set of figures corresponds to the results of the parameter estimation. We have used the Fisher information matrix to estimate expected errors. The results quoted below are obtained only for a single Michelson (X) interferometer. Note that the PhenomC waveform possesses all parameter degeneracies as restricted PN model for the inspiral because it uses only the dominant harmonic, therefore the result for the sky location and for the distance measurement is so poor. It is known that including the higher harmonics and spin precession improves the result obtained here. However, the fact that we include merger and ringdown helps to have larger SNR and propagates the signal to the higher

frequencies. Adding modulation of the signal due to spin-orbital coupling and higher harmonics allows to measure of polarization and breaks degeneracies in the parameter space (but does not add much to SNR). So these results have to be combined with estimates obtained from the inspiral only and interpolated to the case where we have both higher harmonics spin modulation and the merger-ring-down.

The first set of figures gives the overall histograms for the error distribution for two population (for all realizations). All histograms give the relative errors. The two populations used are **LE** for the large seed and efficient accretion (spins always assumed aligned) and **SE** for small seeds and efficient accretion.

Figures 34 (**SE** model) and 35 (**LE** model) compare LISA (magenta) with C2 (blue), C4 (green) and C5 (red). Only sources with  $\text{SNR} > 10$  are included.

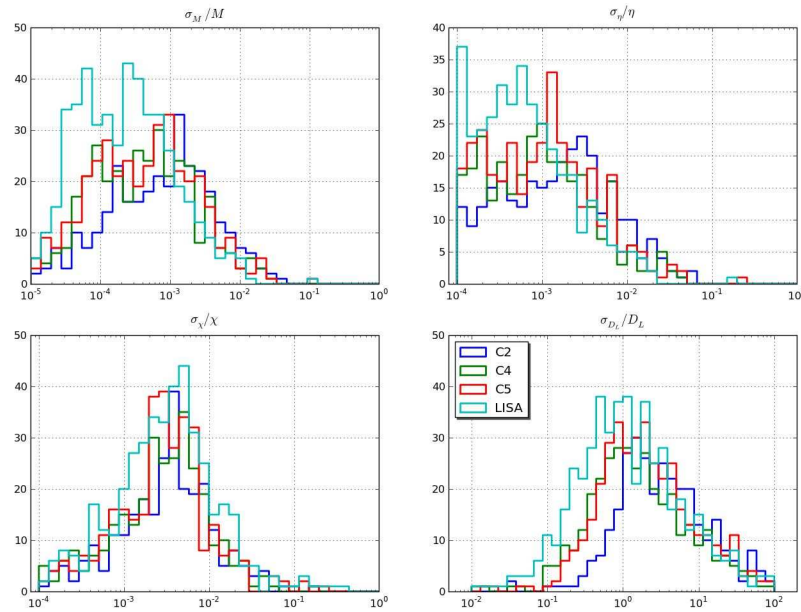


Figure 34:  $1\text{-}\sigma$  errors on source parameters: redshifted mass (upper left); symmetric mass ratio (upper right); spin parameter (lower left); luminosity distance (lower right). Histograms collect all the events in the SE catalogue (small seed), with  $\text{SNR} > 10$ . Light blue histograms are for LISA, blue histograms are for C2, green histograms are for C4 and red histograms are for C5.

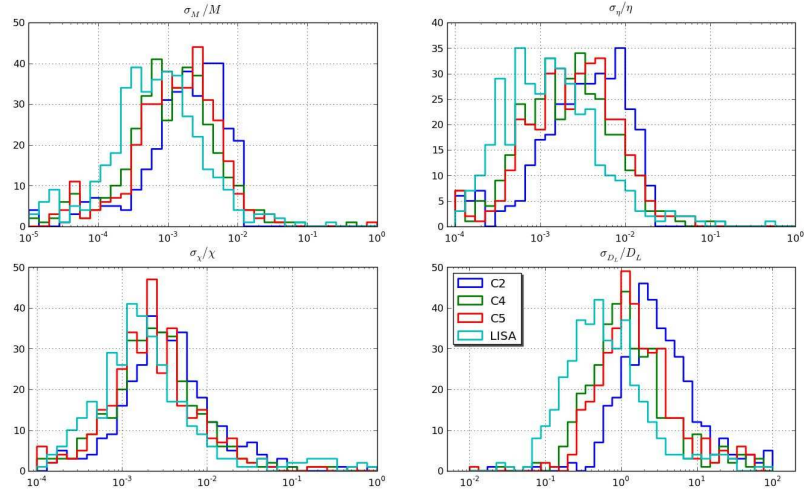


Figure 35: 1- $\sigma$  errors on source parameters. Similar as 34 with LE catalogue (large seed).

In the next set of figures we show the degradation of the performance with the redshift. There we present the median over the realizations value versus the redshift. In the figures 38 (**SE** model) and in 39 (**LE** model) we compare again LISA, C2, C4 and C5 with the same color-coding as in the figures with histograms

The median source SNR with LISA, C2, C4 and C5 as a function of redshift is shown in figures 38-to-39.



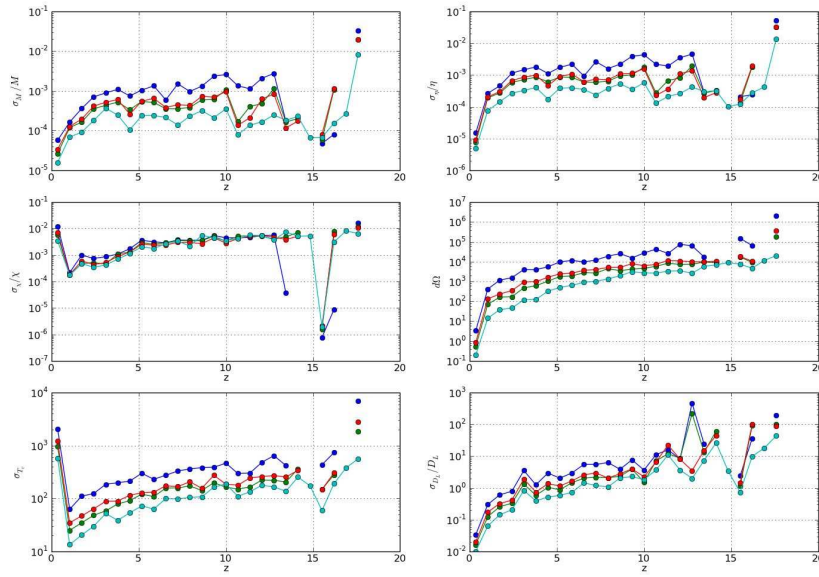


Figure 36: Median 1- $\sigma$  errors on the source parameters as a function of  $z$ : redshifted mass (upper left); symmetric mass ratio (upper right); spin parameter (middle left); sky location in  $\text{deg}^2$  (middle right); coalescence time in seconds (lower left); luminosity distance (lower right). Colorstyle as in figure 34 : light blue histograms are for LISA, blue histograms are for C2, green histograms are for C4 and red histograms are for C5. Model SE (small seeds) is assumed.

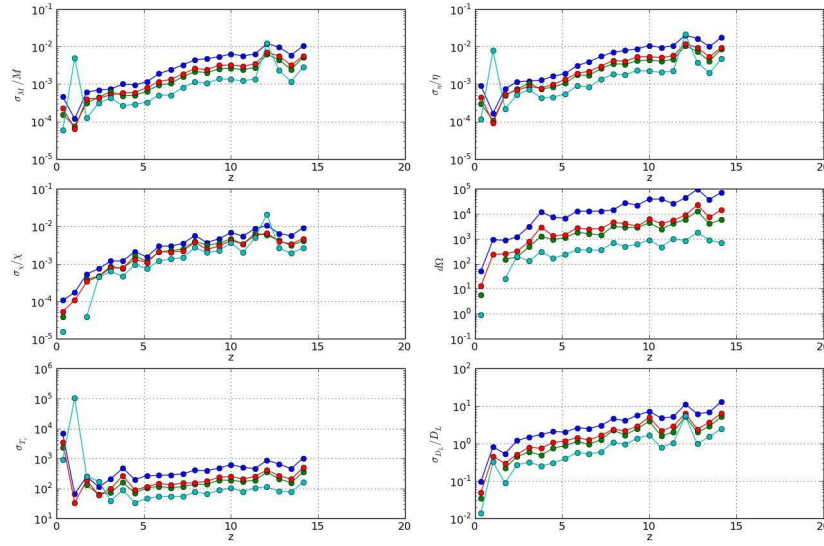


Figure 37: Same as figure 36 but for the LE (large seed) catalogue.

Those curves are not smooth at low and high redshifts. The low redshift end has only few events and observed outliers are effect of low statistic. For high redshift events we again do not have many event but due to low SNR. We also provide the median SNR for **LE** and **SE** models (with the same color-codding) in the figures 39, 38.

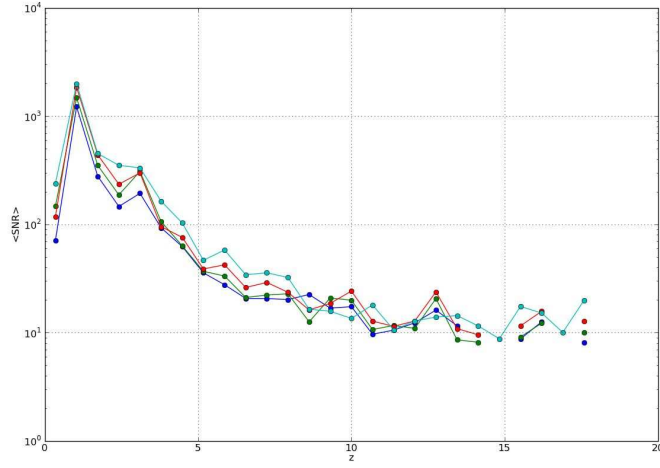


Figure 38: Median SNR  $s$  as a function of  $z$ . Colorstyle as in figure 34 : light blue histograms are for LISA, blue histograms are for C2, green histograms are for C4 and red histograms are for C5. Model SE (small seeds) is assumed.

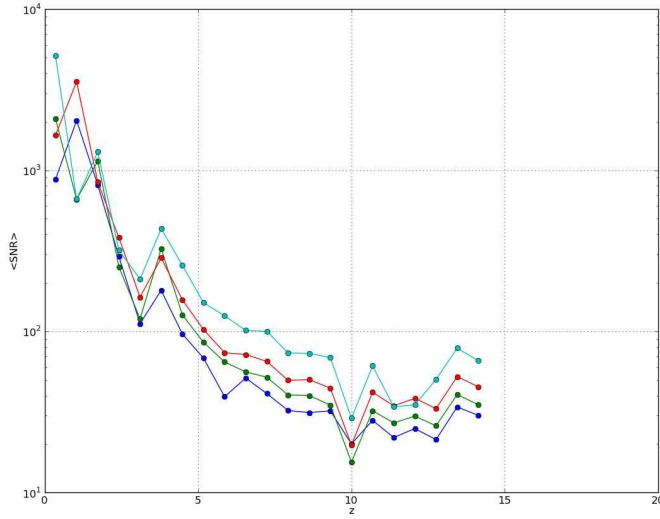


Figure 39: Same as figure 38 but for the LE (large seed) catalogue.

#### 3.4. 4 vs 6 links and low frequency sensitivity impact on the source distance determination (A. Sesana)

This note is a (I hope useful) followup on the discussion we had yesterday about the impact of the number of links and of the low frequency sensitivity on the source

distance (redshift) determination. In each plot I show separately the impact of both, in the attempt of assessing their relative importance. I used the Horizon catalogue, which is a mix of our four 'fiducial' models, and I show histograms with the number of detected sources, averaged over 1000 realizations of the MBH binary population. The errors are computed using inspiral 2PN waveforms, and then rescaled appropriately to account for the increased SNR provided by the merger and ringdown. This is very rough, but the results have been shown by Stas to be consistent with those obtained with PhenomC waveforms. In figure 40 I show the effect on the overall detectable population, assuming a threshold  $\text{SNR} = 8$  (the number of sources therefore is different for each of the configurations). In the top panel I show the progression **LISA 6 links**  $\rightarrow$  **LISA 4 links**  $\rightarrow$  **C2 4 links**; in the bottom panel, instead, I show **LISA 6 links**  $\rightarrow$  **C2 6 links**  $\rightarrow$  **C2 4 links**. In general, both reducing the low frequency sensitivity (i.e. reducing the time spent in band by the source) and cutting 2 links (i.e. losing the capability of reconstructing the two polarizations 'right away') cause a degradation in the redshift (converted from the luminosity distance using standard cosmology) determination of a factor of  $\sim 5$ , in the relevant error range (i.e.  $\text{error} < 100\%$ ). In figure 41 I select sources with total redshifted mass  $> 10^6 M_\odot$ . In this case, both factors contribute to the degradation, with a mild predominance of the low frequency reduced sensitivity. This is because such sources would be observable for a long time during their inspiral, in the LISA configuration, and we lose all that information with the descoped designs. For the low mass sources (total redshifted mass  $< 10^5 M_\odot$ ), the switch to 4 links seems instead to be more catastrophic. This is because, with the LISA design, most of the inspiral of such sources is hidden in the galactic binary confusion noise, and descoping the low frequency sensitivity of the instrument doesn't affect the distance determination too much (compare in particular the black and green curve in the lower panel). Most of the degradation is therefore given by the loss of the polarization information in this case (this is actually different to what we naively thought yesterday).

Note that a C2 configuration with 6 links still gives a useful redshift determination for most of the sources, while the 4 links configuration does not (in particular for light sources at redshift  $> 5$ , see red histograms in figure 42). So, in this respect, keeping 6 links would be important.

LISA gives us distance information through: **(i) constellation motion during the inspiral phase; (ii) polarization reconstruction with the 6 links**. In the 4 links descoped baselines we lose both. So, if with LISA we could get important distance information with relatively cheap waveforms, we can not say the same with the descoped versions.

The information can be restored by including higher harmonics, eccentricity, and spin precession. However their impact has to be properly quantified. Moreover, as Gerard and Stas pointed out, **our ability to determine the source distance is not anymore 'detector dependent' but 'waveform dependent'**, which is, in any case, a risk. For example, if most of the sources have almost perfectly aligned spins, even with the correct waveforms given by Mother Nature, we might not be able to determine the distance of most of them with a 4 links descoped detector; conversely we would be able to do so anyway, with a 6 links LISA-like baseline.

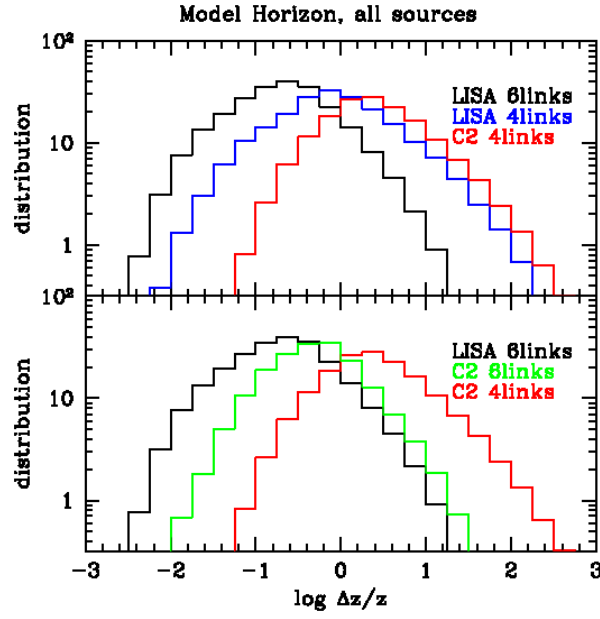


Figure 40: Redshift determination accuracy over all the observable population. Histograms are averaged over 1000 realizations of the horizon models. Legend is given in the panels.

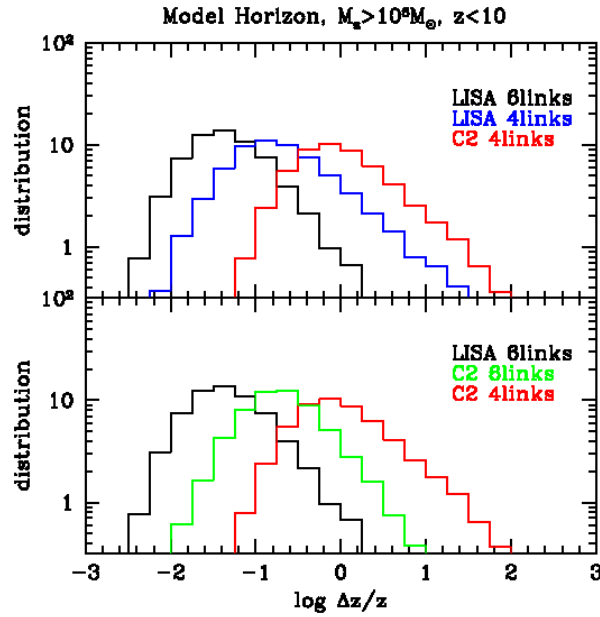


Figure 41: Same as figure 40, but for massive sources only.

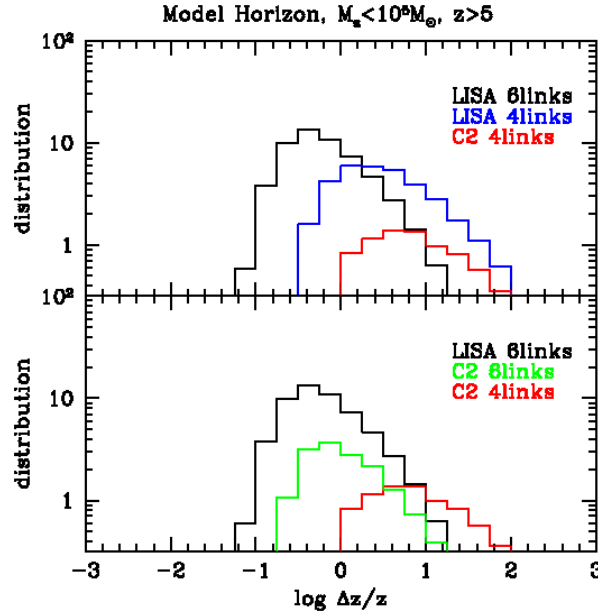


Figure 42: Same as figure 40, but for light sources only.

3.5. *Model selection (Alberto Sesana, Marta Volonteri, Emanuele Berti, Jonathan Gair)*

(‘section captain’: Alberto Sesana)

#### 4. Model Selection

We are performing a model selection study similar to that carried by [?]. The results should be ready within this week. Here we just share some results about the observable massive black hole binary (MBHB) population, and some crude estimation of the errors on source parameters.

In practice we consider the four default models (SE, SC, LE, LC) and a mixed model in which we artificially mixed the SE and the LE model.

- For each detector configuration (LISA, C1, C2, following the standard nomenclature) we compute the transfer function, i.e., the completeness of the detector in the  $(M, q, z)$  parameter space.
- We then filter the intrinsic distribution of merging MBHBs predicted by each model with the appropriate transfer function to produce *theoretically observable* distributions to be compared with observed catalogues.
- We then draw 1000 Montecarlo realizations of each model and simulate observations with LISA, C1 and C2 including Fisher information matrix (FIM) errors. We assume two years of observations for each detector configuration and count only sources coalescing within this timespan. In table 4 we list the number of observable sources for each model and for each detector, assuming different performances (see table caption for details).

- Montecarlo realizations will then be compared to the *theoretically observable* distributions to assess model distinguishability (to be done by Jon these days).

Both the transfer functions and the Montecarlo realizations are computed considering inspiral-merger-ringdown waveforms (IMR) in the following way. Using PhenomC waveforms, Emanuele computed the average ratio  $\mathcal{R} = \text{SNR}_{\text{IMR}}/\text{SNR}_{\text{insp}}$  for sources on a grid of  $(M, q, z)$ . However, 2PN inspiral only waveforms are currently included in our codes for computing the transfer functions and to estimate parameter errors. To compute the transfer function we therefore compute the 2PN  $\text{SNR}_{\text{insp}}$  of each source and we rescale it by the appropriate factor  $\mathcal{R}$ . The same we do for parameter estimation; we used 2PN inspiral waveforms only, and then we rescaled the errors by the appropriate factor  $\mathcal{R}$ . This is a very crude way to proceed, but it was the only practicable one in such a short timescale, and gives reasonable results.

## 5. Observable population and crude error estimation.

We collect here some preliminary plots. Figure 43 shows the marginalized *theoretically observable* distributions, i.e., the intrinsic MBHB coalescence distributions filtered with the appropriate transfer function. Assuming a POPIII model (SE), we loose more than 50% of the events going from classic LISA (black) to configuration C1. Still we have a consistent source population, and a very good chance to get some event out to redshift 11-12. Figure 44 represents the same distributions for a massive seed model (LE), and in this case the number of observable events is much less affected ( $< 20\%$ ). Note that the difference between considering IMR waveforms (thick-dashed) and inspiral only (thin-solid) is minor, and it affects particularly massive, unequal binaries. It turns out infact that considering the merger and ringdown mostly affect the transfer function for massive, unequal binaries, which, in our models, are subdominant.

Figure 45 shows error distributions for configuration C2, assuming a single interferometer and threshold  $\text{SNR}=8$ . Dashed histograms take into account only the inspiral, while the solid ones consider also merger and ringdown (IMR). As expected, there is a mild general improvement in all the errors, when considering IMR. Note the horrendous  $\Delta z/z$ ! in this case 60% of the sources have undetermined redshift (we compute the error on the luminosity distance and we convert it in  $\Delta z/z$  assuming a concordance cosmology). Even though such waveforms are very simplified, and the real situation is probably going to be better than this, there is an indication that a single, descoped interferometer (4 laser links) may be insufficient to decently determine the source luminosity distance/redshift. This is shown also in figure 46, where configurations C1 (red), C2 (blue) and classic LISA (black) are compared. Again we assume a single interferometer with threshold  $\text{SNR}=8$ . There is more than an order of magnitude degradation in the error estimation of many sources, going from LISA to C1. Notice that the error in  $\Delta z/z$  is bad also for LISA. This is because we are considering a single interferometer. The difference between one and two interferometers is shown in figure 47. Here we show classic LISA (black, lower panel) and C1 (red, upper panel), considering one (solid) and two (dashed) interferometers. The histograms are shifted to the left by about a decade, adding a second Michelson. In particular for classic LISA, the typical error is  $\sim 10\%$ , in line with our previous results. Note that few sources (massive, nearby systems) have a  $\Delta z/z < 1\%$ , because of the high SNR given by the addition of the merger and the ringdown to the signal. In the C1 case, adding a second interferometer, would at least

Model	Detector	1 int. SNR= 8	1 int. SNR= 20	2 int. SNR= 8	2 int. SNR= 20
SE	LISA	64.96	40.98	79.73	49.96
	C2	40.09	23.01	49.73	29.89
	C1	32.40	17.79	40.66	23.58
SC	LISA	70.64	46.99	84.76	56.19
	C2	45.63	27.04	55.50	34.99
	C1	37.54	20.84	46.38	27.86
LE	LISA	48.70	46.04	49.19	48.56
	C2	44.94	34.62	47.80	42.11
	C1	41.61	27.50	46.07	35.88
LC	LISA	42.80	40.47	43.16	42.43
	C2	38.72	30.47	41.21	36.00
	C1	35.30	25.04	38.81	31.19

Table 4: Number of *theoretically observable* events in two year of observation, for the four considered models (SE, SC, LE, LC), assuming three different detectors (LISA, C2, C1). The four columns correspond to four different detector performances: a single Michelson with minimal SNR= 8 for trustworthy parameter estimation (column 3); a single Michelson with minimal SNR= 20 for trustworthy parameter estimation (column 4); two Michelson with minimal SNR= 8 for trustworthy parameter estimation (column 5); two Michelson with minimal SNR= 20 for trustworthy parameter estimation (column 6).

allow redshift determination of  $\sim 50\%$  of the sources.

The code used for this model selection exercise, is a restricted PN inspiral, non-spinning code, and it is conservative in the sense that all effects we omitted (IMR, higher-harmonics, spin) should help; however the SNR rescaling should partially account for these omissions. In any case, these plots show how bad is a descoped instrument with a single Michelson for distance determination to the source. It is important to understand if the situation improves significantly by including higher-harmonics, spin, eccentricity, etc. Look forward to some more sophisticated parameter estimation studies (e.g. Neil+Ryan+Scott+Antoine K. for precession+higher harmonics in the inspiral; Sean and NASA Goddard for IMR+higher harmonics, and so on).



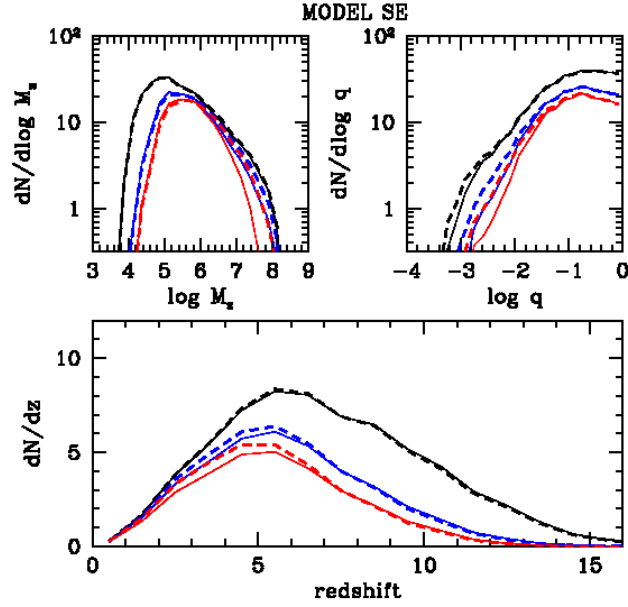


Figure 43: *Theoretically observable* marginalized distributions for model SE. In each panel we plot curves for LISA (black), C2 (blue) and C1 (red). Thick-dashed curves are for IMR waveforms, while thin-solid are for inspiral only. The curves are normalized so that their integrals return the number of observed events in two years. The three panels show the distributions as a function of total redshifted mass ( $M_z = (M_1 + M_2)(1 + z)$ , upper left panel), mass ratio ( $q = M_2/M_1 < 1$ , upper right panel), and redshift ( $z$ , lower panel).

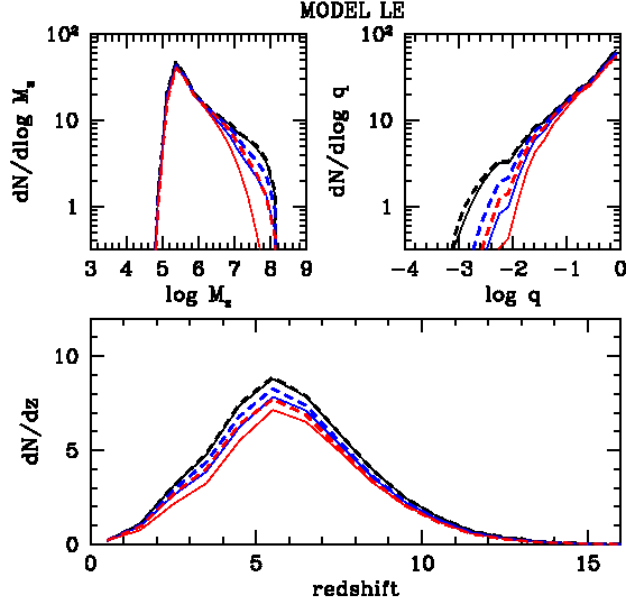


Figure 44: Same as figure 43 but for model LE.

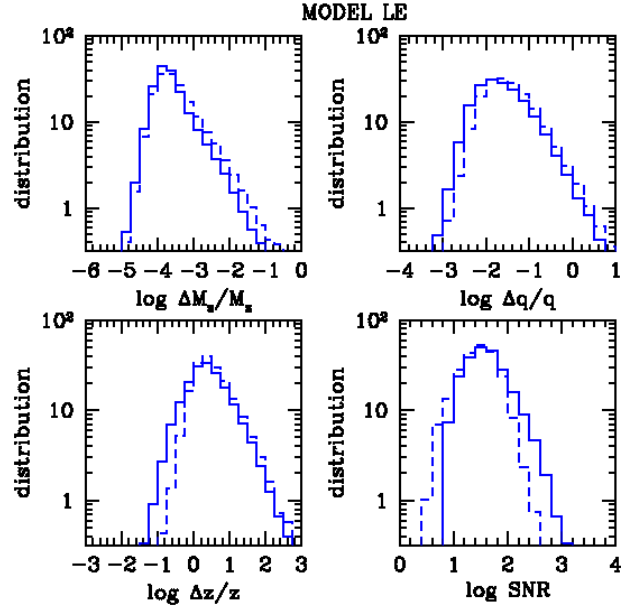


Figure 45:  $1\text{-}\sigma$  errors in the determination of the binary parameters, averaged over 1000 realizations of model LE. Here we assume configuration C2, one Michelson and threshold  $\text{SNR}=8$ . Dashed histograms are for inspiral only, solid ones are for IMR waveforms.

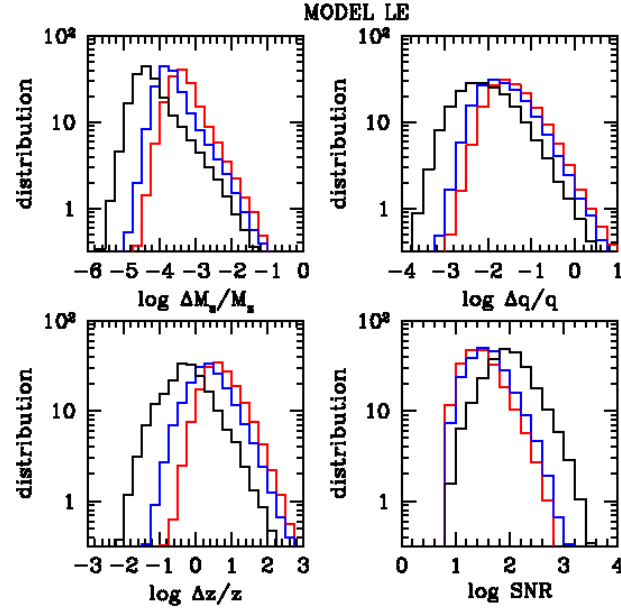


Figure 46:  $1\text{-}\sigma$  errors in the determination of the binary parameters, averaged over 1000 realizations of model LE, assuming different detectors: LISA (black), C2 (blue), C1 (red). We assume one Michelson and threshold  $\text{SNR}=8$

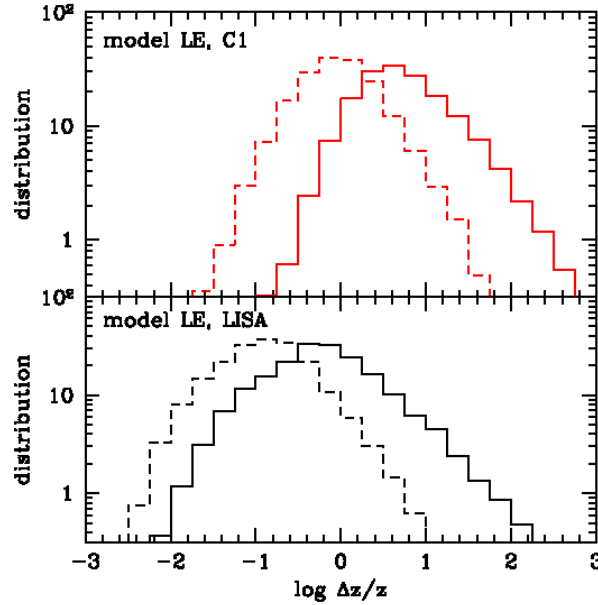


Figure 47:  $1\text{-}\sigma$  errors in the determination of  $z$  for LISA (black, lower panel) and C1 (red, upper panel). Solid and dashed histograms are for one and two Michelson respectively. We averaged over 1000 realizations of model LE, assuming threshold  $\text{SNR}=8$ .

## 6. EMRIs

(‘section captains’ : Jon Gair & Ed Porter)

- [1] Dhurandhar, S. V. and Nayak, K. R. and Koshti, S. and Vinet, J.-Y. *Classical and Quantum Gravity* **22**, 481-487 (2005)
- [2] A. Sesana, M. Volonteri and F. Haardt, *Mon. Not. Roy. Astron. Soc.* **377**, 1711 (2007) [arXiv:astro-ph/0701556].
- [3] M. Volonteri, F. Haardt and P. Madau, *Astrophys. J.* **582**, 559 (2003) [arXiv:astro-ph/0207276].
- [4] S. M. Koushiappas, J. S. Bullock and A. Dekel, *Mon. Not. Roy. Astron. Soc.* **354**, 292 (2004) [arXiv:astro-ph/0311487].
- [5] M. C. Begelman, M. Volonteri and M. J. Rees, *Mon. Not. Roy. Astron. Soc.* **370**, 289 (2006) [arXiv:astro-ph/0602363].
- [6] J. M. Bardeen, *Nature* **226**, 64 (1970).
- [7] K. S. Thorne, *Astrophys. J.* **191**, 507 (1974).
- [8] A. R. King and J. E. Pringle, *Mon. Not. Roy. Astron. Soc. Lett.* **373**, L93 (2006) [arXiv:astro-ph/0609598].
- [9] E. Berti and M. Volonteri, *Astrophys. J.* **684**, 822 (2008) [arXiv:0802.0025].
- [10] T. Bogdanovic, C. S. Reynolds and M. C. Miller, *Astrophys. J. Lett.* **661**, 147 (2007) [arXiv:astro-ph/0703054].
- [11] M. Dotti, M. Volonteri, A. Perego, M. Colpi, M. Ruszkowski, F. Haardt, *Mon. Not. Roy. Astron. Soc.* **402**, 628 (2010).
- [12] J. Cuadra, P. J. Armitage, R. D. Alexander, M. C. Begelman, *Mon. Not. Roy. Astron. Soc.* **393**, 1423 (2009).
- [13] C. Roedig, M. Dotti, A. Sesana, J. Cuadra, M. Colpi, to appear in *Mon. Not. Roy. Astron. Soc.* (2011) [arXiv:astro-ph/1104.3868].
- [14] A. Sesana, *Astrophys. J.* **719**, 851 (2010)
- [15] C. G. Lacey and S. Cole, *Mon. Not. Roy. Astron. Soc.* **262**, 627 (1993).
- [16] W. H. Press and P. Schechter, *Astrophys. J.* **187**, 425 (1974).

- [17] R. K. Sheth and G. Tormen, Mon. Not. Roy. Astron. Soc. **329**, 61 (2002) [arXiv:astro-ph/0105113].
- [18] M. G. Haehnelt, Mon. Not. Roy. Astron. Soc. **269**, 199 (1994) [arXiv:astro-ph/9405032].
- [19] K. Menou, Z. Haiman and V. K. Narayanan, Astrophys. J. **558**, 535 (2001) [arXiv:astro-ph/0101196].
- [20] E. Berti, A. Buonanno, C. M. Will, Phys. Rev. **D71**, 084025 (2005). [gr-qc/0411129].
- [21] L. Santamaria, F. Ohme, P. Ajith, B. Bruegmann, N. Dorband, M. Hannam, S. Husa, P. Mosta *et al.*, Phys. Rev. **D82**, 064016 (2010). [arXiv:1005.3306 [gr-qc]].
- [22] P. Ajith, S. Babak, Y. Chen, M. Hewitson, B. Krishnan, A. M. Sintes, J. T. Whelan, B. Bruegmann *et al.*, Phys. Rev. **D77**, 104017 (2008). [arXiv:0710.2335 [gr-qc]].
- [23] P. Ajith, M. Hannam, S. Husa, Y. Chen, B. Bruegmann, N. Dorband, D. Muller, F. Ohme *et al.*, [arXiv:0909.2867 [gr-qc]].
- [24] E. Berti, V. Cardoso, C. M. Will, Phys. Rev. **D73**, 064030 (2006). [gr-qc/0512160].
- [25] E. E. Flanagan, S. A. Hughes, Phys. Rev. **D57**, 4535-4565 (1998). [gr-qc/9701039].
- [26] E. Berti, V. Cardoso, J. A. Gonzalez, U. Sperhake, M. Hannam, S. Husa, B. Bruegmann, Phys. Rev. **D76**, 064034 (2007). [gr-qc/0703053 [GR-QC]].